Global Biogeochemical Cycles

RESEARCH ARTICLE
10.1029/2021GB007292

Key Points:

- Particle concentration, composition, and size partitioning from three transect cruises are used to estimate mass flux
- Particle sinking velocity is estimated using a modified Stokes' law that incorporates porosity-size power relationships
- The Arctic cruise has lower mass flux than the other two cruises due to high seawater viscosity, small particle sizes and low concentrations

Supporting Information:

Supporting Information may be found in the online version of this article.

Correspondence to:

Y. Xiang,
yaxiang@uw.edu

Citation:

Xiang, Y., Lam, P. J., Burd, A. B., & Hayes, C. T. (2022). Estimating mass flux from size-fractionated filtered particles: Insights into controls on sinking velocities and mass fluxes in recent U.S. GEOTRACES cruises. *Global Biogeochemical Cycles*, *36*, e2021GB007292. https://doi.org/10.1029/2021GB007292

Received 3 JAN 2022
Accepted 25 MAR 2022

Estimating Mass Flux From Size-Fractionated Filtered Particles: Insights Into Controls on Sinking Velocities and Mass Fluxes in Recent U.S. GEOTRACES Cruises

Yang Xiang[1,2], Phoebe J. Lam[1], Adrian B. Burd[3], and Christopher T. Hayes[4]

[1]Department of Ocean Sciences, University of California, Santa Cruz, CA, USA, [2]Cooperative Institute for Climate, Ocean, and Ecosystem Studies, University of Washington, Seattle, WA, USA, [3]Department of Marine Sciences, University of Georgia, Athens, GA, USA, [4]School of Ocean Science and Engineering, University of Southern Mississippi, Stennis Space Center, MS, USA

Abstract We compile full ocean-depth size-fractionated (1–51 and >51 μm) particle concentration and composition of suspended particulate matter from three recent U.S. GEOTRACES cruises, and exploit detailed information of particle characteristics measured to give insights into controls on sinking velocity and mass flux. Our model integrates the concept of fractal scaling into Stokes' Law by incorporating one of two porosity-size power law relationships that result in fractal dimensions of 1.4 and 2.1. The medians of pump-derived total (>1 μm) mass flux in the upper 100 m of gyre stations are 285.1, 609.2, and 99.3 mg/m^2/d in the North Atlantic, Eastern Tropical South Pacific, and Western Arctic Ocean cruises, respectively. In this data set, variations in particle concentration were generally more important than sinking velocity in controlling variations in mass flux. We examine different terms in a Stokes' Law model to explore how variations in particle and water column characteristics from these three cruises affect mass flux. The decomposition of different aspects of the Stokes' relationship sheds light on the lowest total mass flux of the three cruises in the Western Arctic, which could be explained by the Arctic having the lowest particle concentrations as well as the lowest sinking velocities due to having the smallest particle sizes and the most viscous water. This work shows the importance of both particle characteristics and size distribution for mass fluxes, and similar methods can be applied to existing and future size-fractionated filtered particulate measurements to improve our understanding of the biological pump elsewhere.

Plain Language Summary In this study, we compile concentrations and chemical compositions of marine suspended particles from the full water column in three cruises in different ocean basins, and estimate their corresponding mass sinking velocity and flux. Estimating how fast particles sink and the magnitude of particle flux can help us better understand the cycling of elements in the ocean, including carbon. Not surprisingly, we find that places with higher particle concentrations tend to have higher particle flux. Other factors, such as the chemical composition and size of marine particles and viscosity of seawater compete for influence: some mineral phases in particles, characterized by higher densities, provide excess weight to enhance particle flux; in contrast, smaller particles tend to sink more slowly compared to larger particles. In the high-latitude Arctic Ocean, marine particles have high concentrations of ballasting minerals; this alone, however, cannot outcompete the most viscous water, smallest particle size and concentrations, leading to much smaller mass fluxes compared to tropical oceans.

1. Introduction

The marine biological carbon pump (BCP) plays a crucial role in the global carbon cycle by fixing carbon dioxide (CO_2) in the surface water into particulate organic matter (POM), which then sinks into the deep ocean (Kwon et al., 2009; Volk & Hoffert, 1985). Particle dynamics in the water column, including particle remineralization, aggregation, and disaggregation, are of significance in modifying and attenuating POM during sinking (Burd & Jackson, 2002; Jackson, 1990; Lam & Marchal, 2015; Martin et al., 1987). Most of the sinking flux is composed of phytodetrital aggregates, marine snow, and fecal pellets (Alldredge & Silver, 1988; Bishop et al., 1977; Ebersbach & Trull, 2008; Fowler & Knauer, 1986; Laurenceau-Cornec, Trull, Davies, Bray, et al., 2015; Turner, 2015; Wilson et al., 2013). Only a small fraction of POM (∼10%) produced at the surface, however, sinks below mesopelagic regions (Martin et al., 1987).

Conceptually, vertical mass flux is the product of the sinking velocity and particle concentration. While particle flux scales with concentration, it is modulated by variations in sinking speed caused by changes in particle size, shape, and excess density. The importance of particle size on carbon export is apparent from Stokes' Law (Stokes, 1851), which states that the sinking velocity is proportional to the square of particle diameter. Despite being valid only for spherical solid particles at low Reynolds number, Stokes' Law has been widely used to characterize the sinking speed of marine particles (e.g., Cram et al., 2018; Guidi et al., 2008; Laurenceau-Cornec et al., 2020; McCave, 1975; McDonnell & Buesseler, 2010; Omand et al., 2020). Ballast minerals such as $CaCO_3$ and lithogenic particles have been suggested to provide a source of excess density and/or protection, which promote carbon export into the deep ocean (Armstrong et al., 2001; Francois et al., 2002; Klaas & Archer, 2002). Biogenic opal, or biogenic silica, has a higher density than organic matter but a lower density than $CaCO_3$ and lithogenic particles. The incorporation of opal into an aggregate may also increase aggregate porosity (Bach et al., 2016; Francois et al., 2002; Iversen & Ploug, 2010; Lam & Bishop, 2007; Lam et al., 2011; Puigcorbé et al., 2015). Biogenic opal, therefore, is a less efficient ballast mineral compared to $CaCO_3$ and lithogenic minerals. The importance of a ballast effect in the field is still under active debate, however (Aumont et al., 2017; Boyd & Trull, 2007; Henson, Sanders et al., 2012; Lam & Bishop, 2007; Le Moigne et al., 2012; Lee et al., 2009; Rosengard et al., 2015), since indirect ecosystem effects are difficult to disentangle from direct effects of mineral density (Francois et al., 2002; Henson, Lampitt et al., 2012, Henson, Sanders et al., 2012; Lam et al., 2011; Lima et al., 2014).

Measurements of particle concentration and composition in the North Atlantic, Eastern Tropical South Pacific (ETSP), and Western Arctic Ocean have been made in the past decade as part of the U.S. GEOTRACES program (Lam et al., 2015, 2018; Xiang & Lam, 2020). This study uses the particle data from these recent U.S. GEOTRACES cruises and applies mass-size and porosity-size power-law functions to estimate the corresponding size-fractionated sinking velocity and mass flux. The model used here can be adapted to estimate the sinking fluxes of other size-fractionated particulate phases (e.g., POM, $CaCO_3$, opal) and trace metals (e.g., Fe, Cd, Hg) (e.g., Cui et al., 2021), if the assumption is made that each particulate phase sinks together with the bulk particle pool. This approach not only allows the estimation of particle flux from concentration data, but also allows us to examine how variations in particle and water column characteristics from these three cruises affect mass flux.

2. Cruise Tracks and Particle Sampling Method

The data set consists of results from three recent U.S. GEOTRACES cruises (Figure 1). The North Atlantic Zonal Transect (GA03) cruise was completed with two legs in October-November 2010 and October-December 2011 in the subtropical North Atlantic. The Eastern Pacific Zonal Transect (GP16) cruise was completed in the ETSP Ocean in October-December 2013. The U.S. GEOTRACES Arctic cruise (GN01) focused on the Western Arctic Ocean and was conducted in August-October 2015. The cruise track of the GN01 cruise was in a clockwise direction: it first had a northbound leg and then was followed by a southbound leg. Hereafter, the three cruises are referred to by their GEOTRACES cruise identification numbers (GA03, GP16, and GN01) throughout the text.

Size-fractionated particles were all sampled using dual-flow McLane Research in-situ pumps (WTS-LV) using 51 µm pore-size polyester pre-filters upstream of paired 1 µm pore-size quartz fiber Whatman QMA on one flow path and paired 0.8 µm pore-size polyethersulfone Supor™ filters on the other flow path. Large size fraction particles are referred to as "LSF", representing the size fraction of >51 µm, whereas the small size fraction, "SSF", are particles between 1 and 51 µm. Total particles are defined as the sum of both size fractions (Total = LSF + SSF). More details about the cruise hydrography, sample handling and analytical methods of different particle compositions can be found in Lam et al. (2015), Lam et al. (2018), and Xiang and Lam (2020).

3. Calculating Mass Flux and Average Sinking Velocity Using Size-Fractionated Particle Data

The overall mass flux of particles, F (unit: g/m^2/s), is given as the cumulative sum over all size classes and is the integral of F_i, the mass flux for each size bin i (unit: g/m^2/s/µm), between sizes d_1 and d_2:

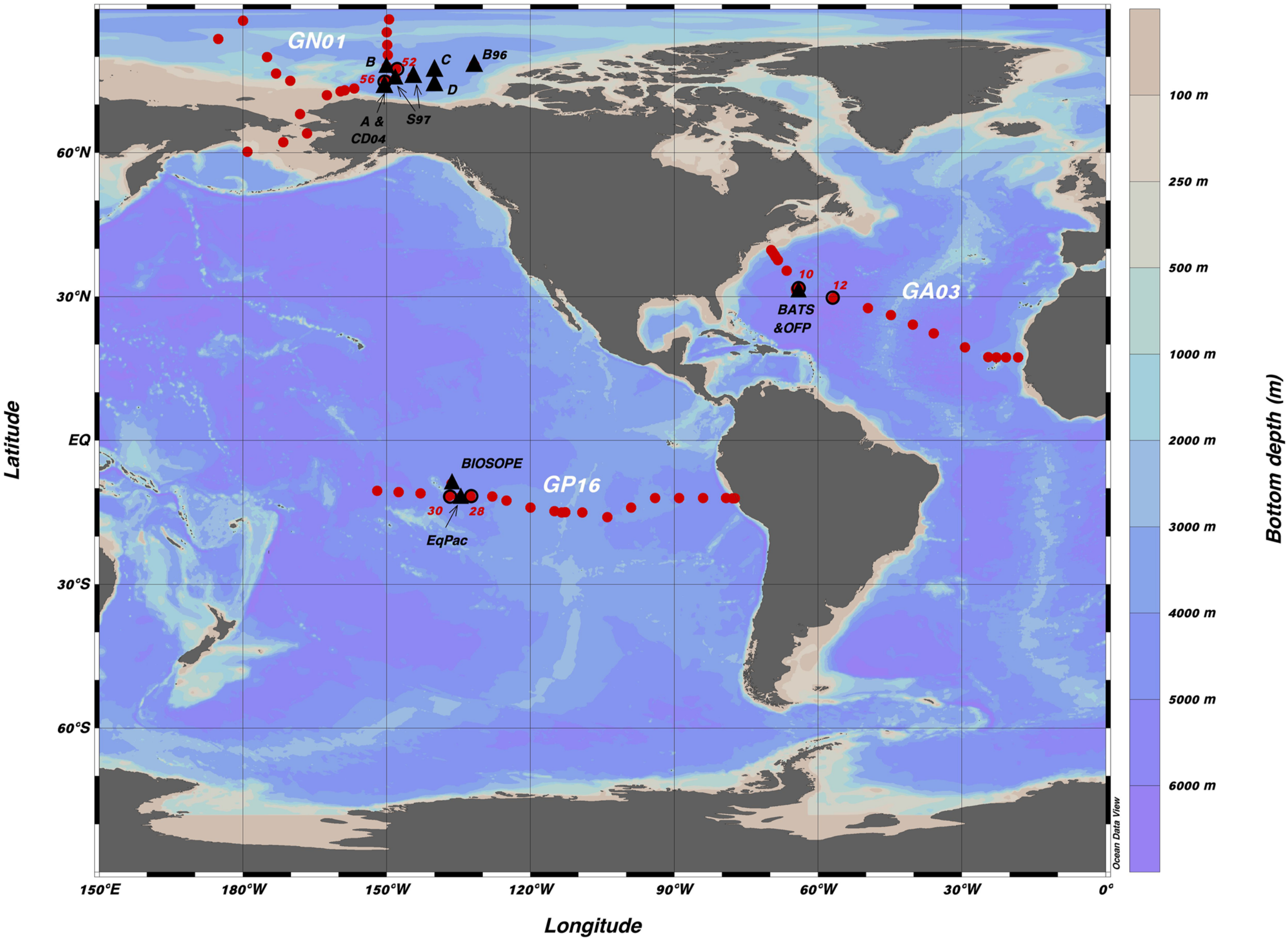

Figure 1. Station map of three U.S. GEOTRACES cruises in which in-situ pump were deployed (red dots). The color bar is ocean bathymetry. The GA03 is the North Atlantic Zonal Transect, GP16 is the Eastern Pacific Zonal Transect, and GN01 is the Arctic cruise. Stations outlined by black circles (GA03: Stations 10 and 12 in leg 2; GP16: Stations 28 and 30; GN01: Stations 52 and 56) are used to compare to nearby sediment trap measurements in the literature (black triangles) that were collected in the same season (±1.5 months) as pump stations. Sediment trap data include the surface-tethered free-drifting cylindrical trap (MultiPITs) deploying for 1–4 days at the BATS (Bermuda Atlantic Time-series Study) from 1988 to 2016 (Steinberg et al., 2001), moored sediment traps in the OFP deploying for more than 12 days at BATS from 1984 to 2017 (Conte, 2019), moored sediment traps deploying for 17–18 days in the Equatorial Pacific (EqPac) Experiment at 12°S and 135°W in the South Pacific in 1992 (Honjo et al., 1995), surface-tethered drifting sediment traps deploying for 1 or 4 days at HNLC stations in the Biogeochemistry and Optics South Pacific Experiment (BIOSOPE) in 2004 (Miquel et al., 2006), surface-tethered sediment traps B96 and S97 deploying for 17 days in the Canada Basin in 1996 and 1997 (Honjo et al., 2010), moored sediment traps CD04 deploying for 16–17 days at 75°N and 150°W in the Canada Basin in 2004 (Honjo et al., 2010), and moored sediment traps A, B, C, and D deploying for 16–17 days in the Canada Basin in 2004, 2007, 2008, and 2010 (Hwang et al., 2015).

$$F = \int_{d_1}^{d_2} F_i \mathrm{dd} = \int_{d_1}^{d_2} \frac{\mathrm{SPM}_i \times W_i}{10^3} \mathrm{dd} \tag{1}$$

The lower integration boundary, d_1, is 1 μm in the SSF or 51 μm in the LSF; the upper integration boundary, d_2, is 51 or 2000 μm for the SSF and LSF, respectively (see Section 3.1). The mass flux spectrum F_i is the product of SPM_i, the suspended particulate mass (SPM) spectrum (unit: g/L/m) in size bin i, and W_i, the sinking velocity (unit: m/s) of particles in size bin i.

To estimate SPM_i, we assume a power-law relationship between particle mass and size (e.g., Alldredge, 1998; Burd et al., 2007), and derive the mass-size power-law relationships for each sample from bulk measurements of particle mass in two size fractions (see Section 3.3). To estimate W_i, we use a Stokes' Law model that assumes the sinking of smooth spherical particles in laminar flow, and incorporate the concept of fractal dimension (e.g., Guidi et al., 2008; Stemmann et al., 2004) through the inclusion of a size-dependent porosity term:

$$W_i = (1 - P_i)\,\frac{g\Delta\rho\left(d_i/10^6\right)^2}{18\eta} \tag{2}$$

where P_i is the particle porosity (unitless) and can be estimated based on a power-law relationship with particle size (Alldredge & Gotschalk, 1988) (Section 3.2.1). The variable d_i is the equivalent spherical diameter of particles for each size bin in µm, g is the gravitational acceleration in m/s^2, $\Delta\rho$ is the excess density of particles over the surrounding seawater in kg/m^3, and η is the dynamic viscosity of seawater in kg/m/s. Excess density $\Delta\rho$ and seawater viscosity η can be calculated directly using particle composition (Section 3.2.2) and seawater hydrography (temperature and salinity) (Section 3.2.3), respectively.

3.1. Particle Size Binning

Both SSF (1–51 µm) and LSF (>51 µm) were evenly divided into 25 bins in logarithmic space. An upper size limit d_2 for the LSF is needed to estimate the mass-size spectra (see Section 3.3) and mass flux (Equation 1). Since sediment traps and camera-based observations suggest that particles of more than 2 mm are often rare in the open ocean (Durkin et al., 2015; Honjo et al., 2008; McDonnell & Buesseler, 2012; Stemmann et al., 2008), we set the upper limit of the LSF to 2 mm for the reference case. The size range and median for each size bin are summarized in Table S1. The center of the bin in log space was used in the calculation of sinking speeds and mass fluxes.

The upper size limit of 2 mm used here is consistent with typical particle sizes collected by in-situ pumps observed by digital and scanning electron microscope images (Lam & Bishop, 2007). While larger aggregates (up to 20 mm) can be observed in productive regions, such as the aggregates from coastal California used in the porosity-size relationship developed by Alldredge and Gotschalk (1988), most stations in this data set are in open ocean regions, where larger aggregates are less expected. The sensitivity of the sinking velocity and mass flux calculations to the choice of this upper limit will be explored in Section 5.1.

3.2. Estimating Particle Sinking Rate for Each Size Bin

3.2.1. Porosity and Size Relationship

Porosity is defined as the volume fraction of an aggregate that is not occupied by solid matter and tends to increase with size in marine aggregates (Alldredge & Gotschalk, 1988). It is an essential parameter in the calculation of particle mass flux and overall volume from size (Jackson et al., 1997; Stemmann et al., 2008). Alldredge and Gotschalk (1988) pioneered porosity measurements in marine aggregates and found a power-law relationship between the porosity and particle size by direct measurements in-situ. This classic power function has been used to calculate the particle sinking velocities in many studies (e.g., Burd et al., 2007; Ruiz, 1997). We used WebPlotDigitizer (Rohatgi, 2010) to extract data points from Alldredge and Gotschalk (1988), and plotted the ordinary least squares relationship between the porosity and particle size in Figure 2 (hereafter A&G88), which is:

$$1 - P_i = \left(8.2\times10^{-3}\right)\times\left(d_i/10^3\right)^{-1.6} \tag{3}$$

In the past 30 years, there have been several additional studies estimating porosity and size of marine aggregates (Bach et al., 2016; Engel et al., 2009; Iversen & Robert, 2015; Lam & Bishop, 2007; Laurenceau-Cornec, Trull, Davies, Christina et al., 2015, 2020; Logan & Alldredge, 1989; Ploug & Passow, 2007; Ploug, Iversen, & Fischer, 2008; Prairie et al., 2015; Schmidt et al., 2014). A detailed summary of all data sources and analytical methods is listed in Table S2. This new compilation includes both aggregates formed in laboratory roller tanks (Shanks & Edmondson, 1989) and natural aggregates (Figure 2). Lam and Bishop (2007) is the only study in this compilation that reported mean porosities for broad size fractions rather than by individual particle size (Table S2), so we used particle size distributions determined optically from nearby cruises (Picheral et al., 2017) to estimate mean particle sizes associated with their estimates of porosities (Text S1 in Supporting Information S1). The porosity-size relationship using ordinary least squares regression for our new compilation (hereafter X22) is:

$$1 - P_i = \left(6.5\times10^{-3}\right)\times\left(d_i/10^3\right)^{-0.87} \tag{4}$$

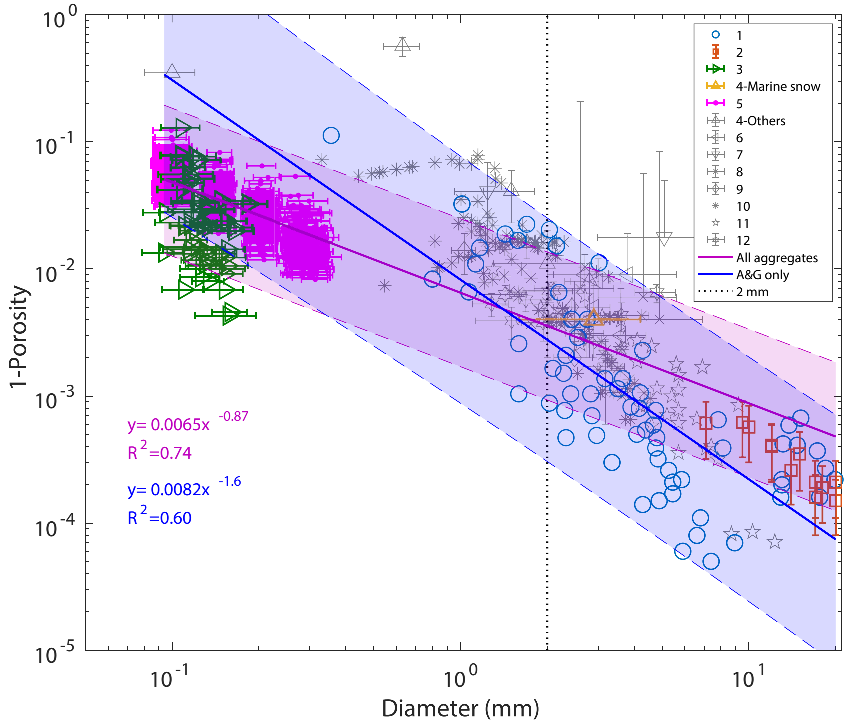

Figure 2. A newly compiled porosity-size relationship from literature. Data points outlined in gray are aggregates formed in laboratory roller tanks, whereas colored symbols are natural marine aggregates. The vertical dotted line is at 2 mm. Solid lines show the ordinary least squares fits to all aggregates (both laboratory-formed and natural) in purple (Equation 4) and Alldredge and Gotschalk (1988) in blue (Equation 3). The purple and blue shaded regions are the 95% prediction interval for each fit, and regression equations are displayed with the colors matching with fit lines. Data sources are 1: Alldredge and Gotschalk (1988); 2: Logan and Alldredge (1989); 3: Lam and Bishop (2007); 4: Ploug, Iversen, and Fischer (2008); 5: Bach et al. (2016); 6: Ploug and Passow (2007); 7: Engel et al. (2009); 8: Schmidt et al. (2014); 9: Prairie et al. (2015); 10: Iversen and Robert (2015); 11: Laurenceau-Cornec, Trull, Davies, Christina, and Blain (2015); 12: Laurenceau-Cornec et al. (2020).

In the A&G88 porosity relationship (Equation 3), porosity extrapolates to 0 when the particle size is about 49.7 μm, which is very close to the size cutoff of 51 μm between the SSF and LSF. For simplicity, we treated all SSF particles as pure solids ($P_i = 0$) and all LSF particles as porous aggregates when using A&G88. For the X22 relationship (Equation 4), porosity is 0 when the particle size is about 3.1 μm. We treated SSF particles smaller than 3.1 μm as pure solids, and particles larger than 3.1 μm (part of SSF and all LSF) as porous aggregates when using X22.

It is clear from the considerable scatter in the porosity-size relationship that there are many more controls on porosity than size alone and that a single power-law fit is an oversimplification. Indeed, this is not surprising given the many mechanisms that produce marine aggregates, including abiotic coagulation and fecal pellet production by a wide variety of animals, as well as the influence of minerals on aggregate characteristics (e.g., Engel et al., 2009). The A&G88 porosity-size relationship (Equation 3) was developed for marine snow aggregates in the Southern California Bight, and reasonably represents the porosity-size relationship for large aggregates greater than 1 mm, including those from more recent roller tank experiments. However, A&G88 overestimates $1\text{-}P_i$ (underestimates P_i) for smaller aggregates (<~0.3 mm). In contrast, the new relationship X22 (Equation 4), which is heavily weighted by small natural aggregates (<400 μm) from a mesocosm study in a Norwegian fjord (Bach et al., 2016), describes smaller aggregates well but overestimates $1\text{-}P_i$ (underestimates P_i) for the larger end of the size range.

Logan and Wilkinson (1990) showed that the relationship between the three-dimensional fractal dimension D_3 and the power exponent b in the porosity-size function was $D_3 = 3 + b$. The value of D_3 gives an intuitive estimation of how much space the solid occupies in three dimensions. A pure solid has a three-dimensional fractal dimension of 3. The fractal dimensions in the A&G88 (Equation 3) and X22 (Equation 4) porosity scenarios are

1.4 and 2.1, respectively, which means that marine particles are more space-filling in the new X22 relationship than those in Alldredge and Gotschalk (1988). It is important to note, however, that the X22 relationship also has a smaller coefficient than the A&G88, with the two porosity-size power-law relationships intersecting at 1.4 mm. Using A&G88 leads to a prediction of a lower porosity for particle sizes less than 1.4 mm but a higher porosity for particles more than 1.4 mm compared to the X22. The fractal dimensions of 1.4 and 2.1 represented by these two porosity-size relationships are in line with the range of 1.3–2.5 estimated for the ocean (Guidi et al., 2008; Jackson et al., 1995, 1997; Kilps et al., 1994; Logan & Wilkinson, 1990).

Since particles collected from the three GEOTRACES expeditions tend to be on the smaller end of the spectrum, we assume an upper size limit of 2 mm and use the new compilation (X22; Equation 4) for our reference calculations. We examine the sensitivity of the flux calculations assuming a larger upper size limit and the A&G88 porosity-size relationship in Section 5.1.

3.2.2. Particle Density Calculation

Major particulate phases of solid marine particles determined for each size fraction include POM, opal, lithogenic materials, calcium carbonate ($CaCO_3$), manganese oxides, and iron oxyhydroxides. The contribution of each particle phase to the overall particle mass, or the compositional fraction, was calculated by normalizing its concentration to SPM. Compositional fractions were calculated separately in the LSF and SSF and used in the calculations of particle density. The density of the solid portion of particles, ρ_{particle}, was calculated as:

$$\rho_{\text{particle}} = \rho_{\text{POM}} f_{\text{POM}} + \rho_{\text{opal}} f_{\text{opal}} + \rho_{\text{Litho}} f_{\text{Litho}} + \rho_{\text{CaCO}_3} f_{\text{CaCO}_3} + \rho_{\text{MnO}_2} f_{\text{MnO}_2} + \rho_{\text{Fe(OH)}_3} f_{\text{Fe(OH)}_3} \quad (5)$$

where ρ_{POM}, ρ_{opal}, ρ_{Litho}, ρ_{CaCO_3}, ρ_{MnO_2}, $\rho_{\text{Fe(OH)}_3}$ are the densities of each particle phase, and f_{POM}, f_{opal}, f_{Litho}, f_{CaCO_3}, f_{MnO_2}, $f_{\text{Fe(OH)}_3}$ are the compositional fractions (by weight) of each particle phase. We use a density of POM ρ_{POM} of 1.05 g/cm^3 (Young, 1994), ρ_{opal} of 2.0 g/cm^3 (Hurd & Theyer, 1977), ρ_{Litho} of 2.70 g/cm^3 (Rixen et al., 2019), ρ_{CaCO_3} of 2.71 g/cm^3, ρ_{MnO_2} of 3.0 g/cm^3, and $\rho_{\text{Fe(OH)}_3}$ of 3.96 g/cm^3 (Towe & Bradley, 1967).

Importantly, since we only have bulk composition information available for the SSF and LSF fractions, we assumed that all 25 bins in each size fraction have the same particle composition, and thereby the same particle densities. Indeed, different particle phases (Andrews et al., 2010; Reynolds et al., 2016; Woźniak et al., 2010), and phytoplankton communities (Green, Sosik, Olson et al., 2003, Green, Sosik, Olson, DuRand et al., 2003; Smyth et al., 2019; Stramski et al., 2001) have distinct size distributions, and their corresponding peaks in particle number concentrations do not often occur at the same size. For example, relatively dense lithogenic particles and $CaCO_3$ coccoliths are likely concentrated in the smaller size bins of the SSF spectrum (e.g., Baumann & Sprengel, 2000; Rea & Hovan, 1995) rather than distributed evenly throughout. Thus, the assumption of constant composition in all size bins within each size fraction necessarily results in monotonic changes in sinking velocity with size in the LSF or SSF that might not exist. Using an average bulk composition would lead to an overestimate of true mass flux if denser particle phases were skewed to smaller particles. Unfortunately, measuring particle composition at each size bin is not currently possible with existing sampling and analytical techniques. The use of a single bulk composition is common practice (e.g., Bach et al., 2016) for calculating the sinking velocity of marine aggregates. Here, we measure bulk composition and thus density in two size fractions (SSF and LSF) to estimate the mass flux in each of these size fractions.

3.2.3. Seawater Potential Density and Viscosity

Hydrographic data, such as temperature, salinity, dissolved oxygen, and nutrients, were measured during each cruise (Cutter et al., 2019; Schlitzer et al., 2018). Temperature, salinity, and pressure from the conductivity/temperature/depth bottle data were interpolated linearly to pump depths. The seawater density and gravitational acceleration were calculated using the Thermodynamic Equation of Seawater-2010 (McDougall & Barker, 2011) in MATLAB (MathWorks Inc.). The seawater density is a function of temperature, salinity, and pressure, and the gravitational acceleration was derived from latitude and pressure. The seawater viscosity was calculated from temperature and salinity following Millero (1974).

3.2.4. Limitations of Using Stokes' Law in Natural Environments

One of the key assumptions in this study is that we assume the sinking of particles obeys Stokes' Law in natural environments. However, the Stokes' Law is only valid at low Reynolds number (Re) in the laminar flow regime, empirically found at Re < 0.5 (White, 1974). Although typical Re values associated with marine aggregates

10.1029/2021GB007292

are 0.4–50 (Alldredge & Gotschalk, 1988; Laurenceau-Cornec et al., 2020), Stokes' Law is potentially valid at higher Reynolds numbers (1 < Re < 50) with the consideration of increasing porosity with size and the presence of mineral contents (Laurenceau-Cornec et al., 2020). Indeed, roller-tank aggregates with minerals were best modeled using Stokes' Law with constant and high porosity (99%), but also well described with a form of Stokes' Law modified with a fractal-porosity relationship and fractal dimension 1.8 (Laurenceau-Cornec et al., 2020), similar to our Equations 3 and 4 with fractal dimensions of 1.4 and 2.1, respectively. For aggregates without minerals, the modified Stokes' law with a fractal-porosity relationship and fractal dimension 1.4 modeled the sinking velocity much better than using constant porosity in Laurenceau-Cornec et al. (2020).

The assumption of spherical particles for our Stokes' Law calculations is a simplification, as marine aggregates are not perfect spheres (e.g., Alldredge & Gotschalk, 1988; Engel et al., 2009; McDonnell & Buesseler, 2010). Given the same size and excess density, irregularly shaped aggregates are characterized by lower sinking velocities than spherical ones due to the increased drag (Alldredge & Gotschalk, 1988).

Another assumption we made in the Stokes' Law calculation is that the flow through the porous aggregate is negligible so that we can apply Equations 3 and 4. The numerical simulations from Kiørboe et al. (2001) suggested that flow occurs in a thin layer at the surface of aggregates, which is borne out by oxygen microsensor measurements within aggregates (Ploug, Iversen, Koski et al., 2008).

Finally, the presence of transparent exopolymer particles (TEP) can also influence the excess density in sinking velocity estimations. Indeed, much of the space in the porous fraction of aggregates can be occupied by TEP (Ploug & Passow, 2007). TEP is operationally defined as >0.4 μm particles filtered by polycarbonate filters that stain with Alcian Blue (Alldredge et al., 1993; Passow, 2002). The density of TEP is 0.70–0.84 g/cm^3, lower than that of seawater (Azetsu-Scott & Passow, 2004). As TEP measurements were not made in our samples, we did not consider its possible influence, but it would be expected to decrease the mass flux estimation.

We consider these limitations in applying Stokes' Law to in-situ pumped particle samples when we compare our estimates to independent measures of mass flux and sinking velocity.

3.3. Estimating Particle Mass Concentration for Each Size Bin

SPM concentrations in the SSF and LSF were measured in the three cruises (Lam et al., 2015, 2018; Xiang & Lam, 2020). The mass partitioning of particles between the two measured size fractions is assessed as f_SSF = $\frac{\text{SSF SPM}}{\text{Total SPM}}$, with a higher f_SSF corresponding to a higher abundance of small particles, or f_LSF = $\frac{\text{LSF SPM}}{\text{Total SPM}}$, which is 1-$f$_SSF. To estimate the SPM spectrum SPM$_i$ in each size bin i, we assume a power-law relationship between mass and size:

$$\text{SPM}_i = \text{pd}_i^{-q} \tag{6}$$

where p and q are constant parameters that are determined from the size-fractionated SPM data (unit: g/m^3) for each sample:

$$\text{SPM} = \frac{\int_{d_1}^{d_2} \text{pd}_i^{-q}\text{dd}}{10^3} \tag{7}$$

For SPM in the SSF, d_1 and d_2 are 1 and 51 μm; for SPM in the LSF, d_1 and d_2 are 51 μm and 2 mm. We fitted a power law distribution for the spectrum and calculated p and q using the measured SSF and LSF SPM. The constants p and q are solved for using the Levenberg-Marquardt algorithm in fsolve in MATLAB (https://github.com/BurdLab/size-spectra-fit). A higher f_SSF is associated with a larger q.

Although the in-situ masses of individual particles are hard to measure, several lines of evidence suggest that individual particle mass (m_i) should scale as a power-law with particle size. Alldredge (1998) showed that the mass of individual marine snow particles collected off the coast of California scaled as a power-law of particle size. Additionally, for particles that can be described using a fractal scaling relationship (as is assumed here), the mass of particles scale as the product of the mass of the smallest particle and a power-law of particle size (e.g., Burd et al., 2007; Cram et al., 2018). Real marine particles are composed of multiple types of particles

10.1029/2021GB007292

(e.g., marine aggregates and fecal pellets), making a fractal scaling of mass a simplification. Nonetheless, the results from Alldredge (1998) show this to be a reasonable simplification. Since the particle number spectrum is also frequently approximated as a power-law function (e.g., Jackson et al., 1997; Loisel et al., 2006; Roullier et al., 2014; Stemmann et al., 2004; Stemmann et al., 2008), the particle mass spectrum, SPM_i, which is the product of the change in mass of a particle with size (m_i) and the number spectrum of particles (n_i), must also be a power law (Burd et al., 2007).

We recognize that applying a single slope to the entire particle mass spectrum is likely an oversimplification for the complex natural assemblage of particles. Nonetheless, it is informative to investigate whether or not these assumptions can capture the first order distribution of particle mass in our observations.

3.4. Estimating Mass-Weighted Average Sinking Velocity in the SSF, LSF, and Total Particles

We incorporate each of the porosity-size power-law relationships (Equations 3 and 4) into Equation 2 to calculate the sinking velocity of particles in size bin i, W_i:

$$W_i = 5.2 \times 10^{-10} \times \frac{g\Delta\rho(d_i)^{0.4}}{18\eta} \tag{8}$$

$$W_i = 2.6 \times 10^{-12} \times \frac{g\Delta\rho(d_i)^{1.1}}{18\eta} \tag{9}$$

The consideration of porosity ($1\text{-}P_i \propto d_i^{-1.6}$ or $1\text{-}P_i \propto d_i^{-0.87}$ in Equations 8 and 9, respectively) decreases the dependence of sinking velocities on the particle size ($W_i \propto d_i^{0.4}$ or $W_i \propto d_i^{1.1}$) compared to the square dependence of W_i on d_i in Stokes' Law (Equation 2) without consideration of porosity ($1\text{-}\ P_i = 1$). As a result, the influence of other parameters, such as the excess density and viscosity, becomes relatively more important.

The mass fraction of each size bin was used to weight the velocity of each size bin to calculate a mass-weighted average sinking velocity (WSV, in m/s). The WSV was computed separately for the SSF (1–51 μm), the LSF (51–2000 μm), and total particles (1–2000 μm) as:

$$\text{WSV} = \int_{d_1}^{d_2} \frac{\text{SPM}_i \times W_i \text{dd}}{\int_{d_1}^{d_2} \text{SPM}_i \text{dd}} \tag{10}$$

3.5. Estimating Mass Flux in the SSF, LSF, and Total Particles

The overall mass flux F is the integration of the mass flux spectrum F_i, as shown in Equation 1, substituting in the appropriate expression for SPM_i (Equation 6) and W_i (Equation 8 or 9) depending on the porosity-size relationship used.

$$F = \int_{d_1}^{d_2} 5.2 \times 10^{-13} \times \frac{pg\Delta\rho(d_i)^{0.4-q}}{18\eta} \text{dd} \tag{11}$$

$$F = \int_{d_1}^{d_2} 2.6 \times 10^{-15} \times \frac{pg\Delta\rho(d_i)^{1.1-q}}{18\eta} \text{dd} \tag{12}$$

To convert $g/m^2/s$ to $g/m^2/day$, one needs to multiply by 86,400 s/day. The SSF and LSF mass flux were calculated separately for each sample using different size boundaries (SSF: 1–51 μm; LSF: 51–2,000 μm) and densities (SSF density vs. LSF density). The total (TOT) mass flux for all (1–2,000 μm) particles is the sum of SSF and LSF fluxes (TOT mass flux = SSF mass flux + LSF mass flux).

The mass flux F of the SSF, LSF, or total particles can also be calculated as the product of the WSV and SPM concentrations of the respective size fraction:

$$F = \text{WSV} \times \text{SPM} \tag{13}$$

Estimated mass flux and WSV in all size fractions (SSF, LSF, and TOT) from the three cruises using two porosity-size relationships are summarized in Table S3.

3.6. Error Estimations

The main sources of error in the calculations of particle sinking velocity and mass flux are from uncertainties in estimated particle density, and the porosity-size and mass-size power-law relationships. It is assumed that there are no analytical errors in the density of particle phase endmembers, temperature, salinity, and other hydrographic parameters (seawater density and viscosity). Errors in particle densities were estimated from propagating errors (1 standard deviation) in the measurements of each compositional fraction. Errors in the porosity-size relationships were estimated from the standard deviations of the regression coefficient (Equation 3: mean ± s.d. = $8.2 \times 10^{-3} \pm 2.1 \times 10^{-3}$; Equation 4: $6.5 \times 10^{-3} \pm 1.6 \times 10^{-4}$) and exponent (Equation 3: mean ± s.d. = -1.6 ± 0.16; Equation 4: $-8.7 \times 10^{-1} \pm 1.5 \times 10^{-2}$). Errors in the coefficient p and exponent q in the mass-size relationship were calculated using a Monte Carlo simulation (https://github.com/BurdLab/size-spectra-fit) using 1,000 runs for each data point (increasing the number of runs to 10,000 produced no appreciable difference in results). For each individual power-law fit for the mass-size spectrum, the masses were picked randomly from a normal distribution having the mean and standard deviation of the measured data. The calculation was repeated for each individual pair of measured size-fractionated SPM data. The distribution of exponent q in each cruise is illustrated in Figure S1 in Supporting Information S1, and the values of q together with errors are visualized in Figure S2 in Supporting Information S1. The overall errors of mass flux and weighted average sinking rate were estimated using a Monte Carlo simulation (10,000 runs) with the assumption that all parameters with errors (particle density, coefficients and exponents of the porosity-size and mass-size power-law relationships) are defined by a normal distribution. All errors are reported in Table S3.

3.7. Comparisons to Related Approaches Using Particle Number Size Spectra to Estimate Mass Flux

Many field and modeling studies estimate particle mass flux according to:

$$F = \int_{D_S}^{D_L} n(d)m(d)w(d)\mathrm{dd} \tag{14}$$

which describes particle flux F as the product of the number spectrum ($n(d)$), mass ($m(d)$), and sinking rate ($w(d)$) of individual particles integrated from the smallest (D_S) to the largest D_L particle sizes (e.g., Cram et al., 2018; Guidi et al., 2008; Guidi et al., 2016). Guidi et al. (2008) used measured particle number spectra ($n(d)$) from the Underwater Video Profiler (UVP) together with measured mass fluxes from 108 paired sediment traps to solve for the best fit parameters that described an assumed power-law relationship for $m(d)w(d) = Ad^b$. The empirically derived $m(d)w(d)$ was then applied to over 1,200 UVP profiles to estimate mass flux more broadly. In a model study, Cram et al. (2018) followed a similar approach to Guidi et al. (2008), assuming a constant fractal dimension of 2.3 as estimated by Guidi et al. (2008) to estimate $m(d)$ and $w(d)$ and using a one-dimensional particle sinking and remineralization model that explicitly simulates a complete number spectrum of particles ($n(d)$). Here, we use measured size-fractionated particle mass to estimate $n(d)\times m(d)$ (SPM_i in Equation 6) and use an updated porosity-size relationship and Stokes' Law to estimate $w(d)$ (Equations 8 and 9).

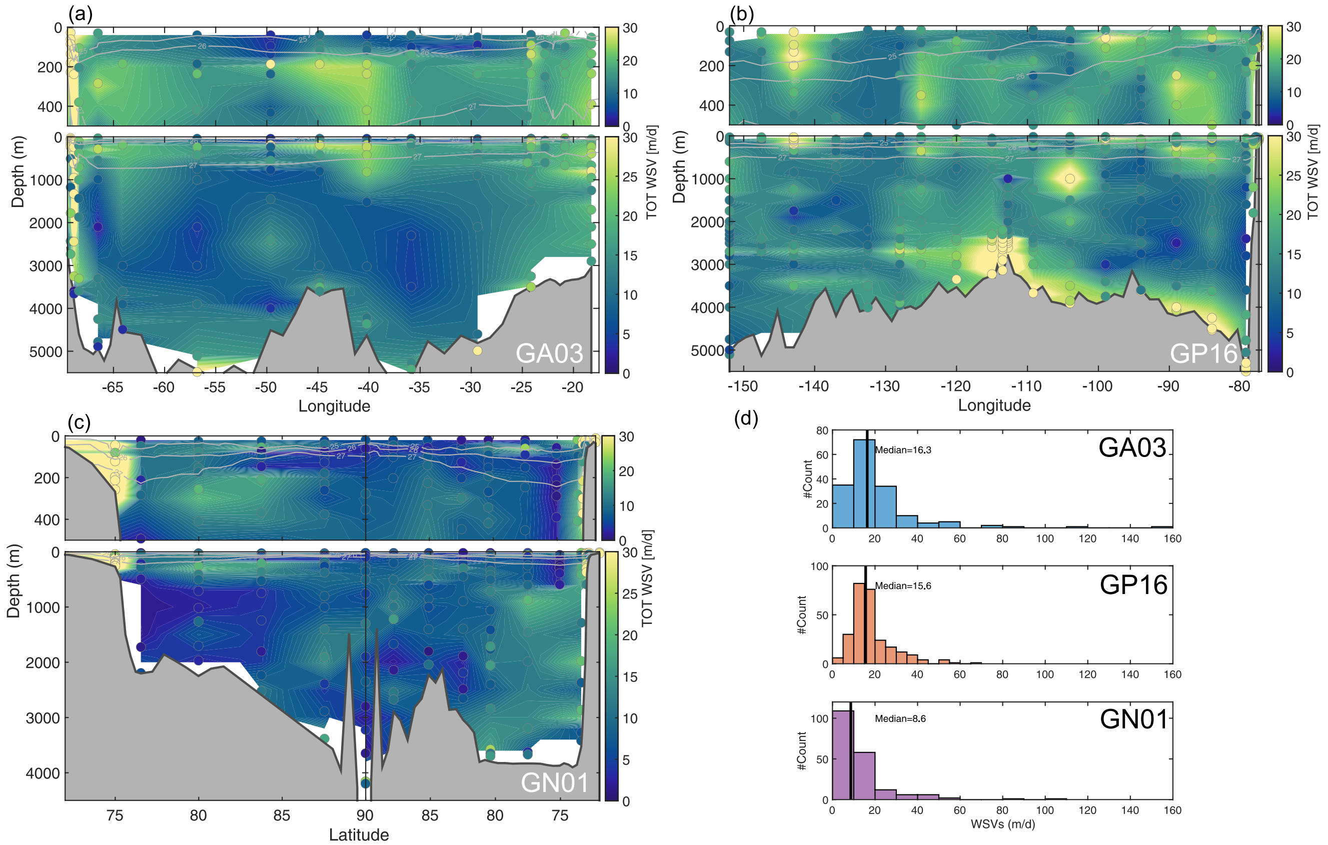

Figure 3. Section plots and histograms of estimated mass-weighted average sinking velocity (unit: m/d) for TOT (1–2000 μm) particles in three cruises. (a): GA03 section plot; (b): GP16 section plot; (c) GN01 section plot; (d) histograms for all cruises. These estimations are from the reference scenario, using X22 (Equation 4) as the porosity-size relationship and 2 mm as the upper size limit for the LSF. Thick gray contours in (a)–(c) are potential density anomaly of 25, 26 and 27 kg/m^3, and thin white lines are 50 evenly spaced contour lines within the range of the color scale. Vertical solid lines in (d) are the median mass-weighted average sinking velocity in each cruise.

4. Estimated Average Sinking Velocity and Mass Flux in the Three Cruises

The mass fluxes and sinking velocities calculated using an upper size limit of 2 mm and the new X22 porosity-size relationship (Equation 4) will be first discussed in Sections 4.1 and 4.2 as the reference case. A discussion of sensitivity tests of mass fluxes to a larger upper size limit and to using the A&G88 porosity-size relationship (Equation 3) will be presented in Section 5.1.

4.1. Mass-Weighted Average Sinking Velocity Estimates

Overall, the total mass-weighted average sinking velocities (TOT WSV*s*) in GN01 are significantly lower than the other two cruises (Mann-Whitey U test; $p \ll 0.001$). Median (interquartile range) SSF WSV*s* (unit: m/d) are 1.1 (0.9–1.3), 0.8 (0.7–1.0), and 0.6 (0.4–0.8) in the GA03, GP16, and GN01, respectively (Table S4). Median (interquartile range) LSF WSV*s* (unit: m/d) are 67.9 (50.6–85.4), 69.2 (58.3–81.2), and 50.0 (40.7–64.8) in the GA03, GP16, and GN01, respectively (Table S4). Estimated TOT WSV*s* (unit: m/d) have median (interquartile range) of 16.2 (11.0–23.5) in GA03, 15.5 (11.5–20.5) in GP16, and 8.6 (5.4–13.3) in GN01 (Figure 3d; Table S4).

The magnitude of WSV*s* for each size fraction is determined by the mass size spectrum and sinking velocity for each size bin (Equation 10). Sinking velocities, in turn, are dependent on the hydrography, particle composition, and size (Equation 2). Both GA03 and GN01 are characterized by high TOT WSV*s* near the continental margins. High TOT WSV*s* are also observed in the East Pacific Rise (EPR) hydrothermal plume and near the seafloor in the eastern half of GP16 (Figure 3). In contrast, the benthic nepheloid layers (BNLs) along the deep western

10.1029/2021GB007292

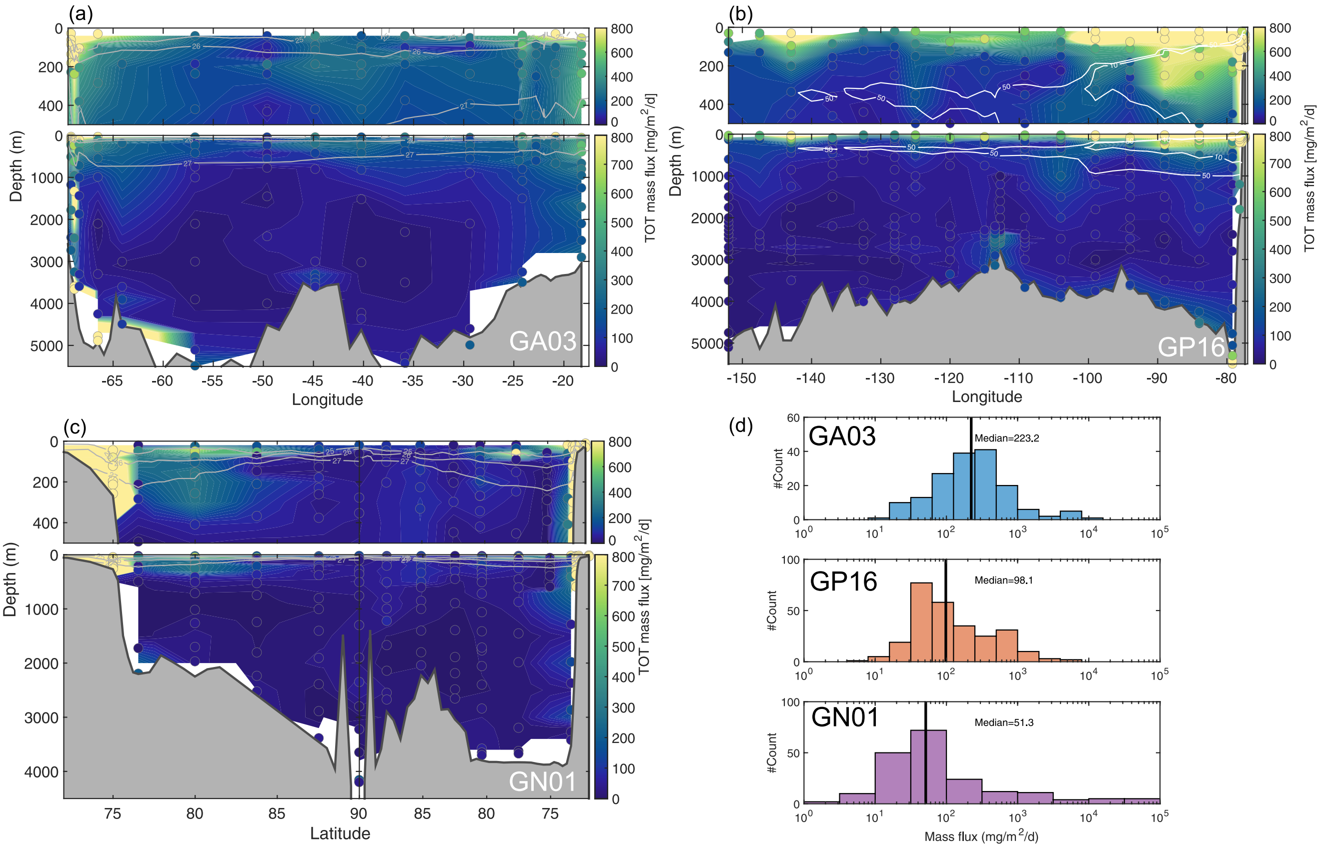

Figure 4. Section plots and histograms of estimated mass flux (unit: mg/m^2/d) for TOT (1–2000 μm) particles in three cruises. (a): GA03 section plot; (b): GP16 section plot; (c) GN01 section plot; (d) histograms for all cruises. These estimations are from the reference scenario, using X22 (Equation 4) as the porosity-size relationship and 2 mm as the upper size limit for the LSF. Thick white contours in (b) are dissolved oxygen concentrations of 10 and 50 μmol/kg. Note that the *x* axes in (d) are logarithmic and vertical solid lines are the median mass flux in each cruise.

boundary of GA03 have TOT WSV*s* at Station 4 (38.3°N, 68.9°W) that are lower than the midwater column values despite much higher fractions of lithogenic content (Figure 3a). These patterns of WSV*s* can be largely explained by the mass size distributions, with distributions favoring larger particles (smaller mass-size exponent *q*) characterizing the high WSV*s* of the margins of GA03 and GN01, the EPR plume, and BNL of the eastern GP16 section, and distributions favoring smaller particles (larger *q*) characterizing the slower WSV*s* of the GA03 BNLs (Figure S1 in Supporting Information S1). Within the near-field EPR hydrothermal plume (<80 km from the ridge axis) in the GP16 cruise, high particle densities from the high oxide fraction (Figure S3 in Supporting Information S1) further increase WSV*s*, with the TOT WSV*s* reaching more than 50 m/d (Figure 3b).

4.2. Mass Flux Estimates

Overall, the GN01 cruise has the lowest TOT mass flux compared to the GA03 and GP16 cruises ($p \ll 0.001$), but also the largest range: both the lowest (Western Arctic Basin) and highest (Chukchi Shelf) mass fluxes of the entire data set are found in the GN01 cruise (Figures 4c-4d), reaching as high as 9.1×10^4 mg/m^2/d. Median (interquartile range) TOT mass flux (unit: mg/m^2/d) is 228.0 (111.0–421.7) in GA03, 97.6 (51.7–281.4) in GP16, and 51.1 (25.4–169.6) in GN01 (Figure 4d; Table S4).

TOT mass fluxes generally decrease with depth and away from the margins (Figure 4). It is interesting that high mass fluxes in the upper 500 m near the Peru margin persist hundreds of kilometers offshore in the GP16 cruise, remaining elevated within the 10 μmol/kg dissolved oxygen contour line (Figure 4b). The low attenuation of mass flux in this low oxygen region is consistent with conclusions drawn from other tracers from the same cruise, such

10.1029/2021GB007292

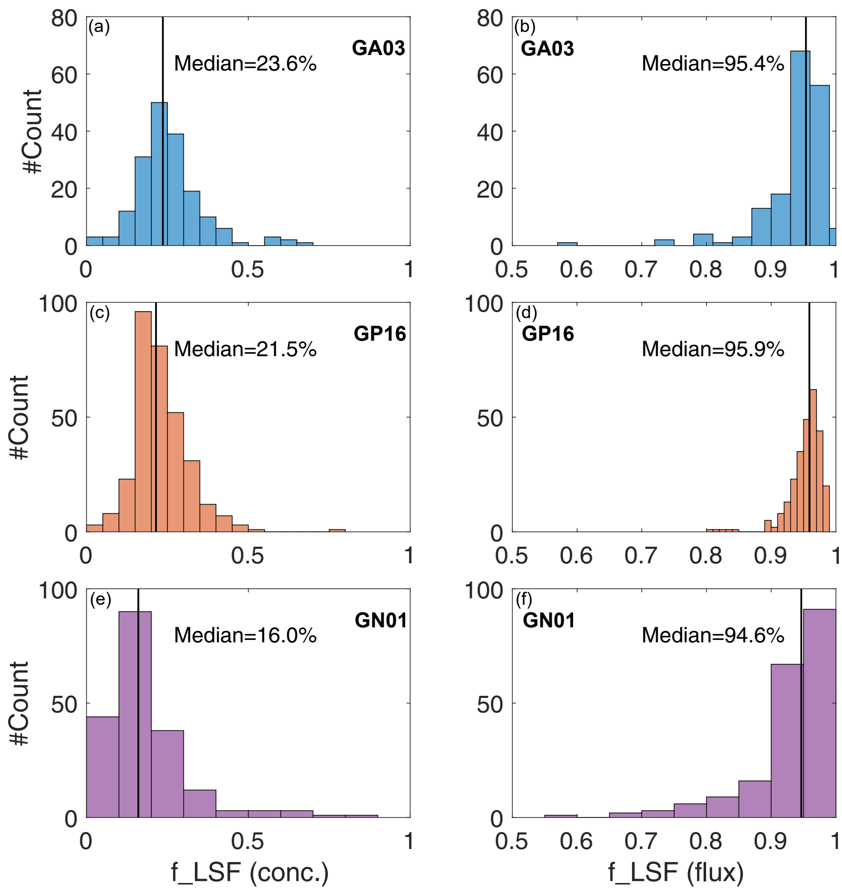

Figure 5. Histograms of mass concentration and flux partitioning in three cruises for the reference scenario. (a): GA03 *f*_LSF (concentration); (b): GA03 *f*_LSF (flux); (c): GP16 *f*_LSF (concentration); (d): GP16 *f*_LSF (flux); (e): GN01 *f*_LSF (concentration); (f): GN01 *f*_LSF (flux). Vertical solid lines indicate the median of each parameter in each cruise.

as the ^{230}Th-normalized POC flux and stable isotope of nitrate ($\delta^{15}N_{NO3}$), which both point to less POC regeneration within the Peru oxygen deficient zone (Pavia et al., 2019; Peters et al., 2018).

4.3. Size-Partitioning of Particle Concentration and Flux

Large, fast-sinking particles often dominate the mass flux into the ocean interior (e.g., Bishop et al., 1977; Fowler & Knauer, 1986; McCave, 1975; Michaels & Silver, 1988). Bishop et al. (1977) used Stokes' Law and particle composition data from large-volume filtration to estimate the size-fractionated mass flux in the upper 400 m of the equatorial Atlantic Ocean, and concluded that large particles (>53 μm) particles account for more than 98% of the total mass flux.

The method used here is similar to Bishop et al. (1977), except that we account for porosity using porosity-size relationships, whereas Bishop et al. (1977) implicitly accounted for porosity in their estimates of excess density of different types of particles. In this data set, the median (interquartile range) of estimated SSF mass flux (unit: mg/m^2/d) is 10.1 (6.7–15.5), 4.1 (2.6–9.2), and 2.9 (1.8–5.2) in the GA03, GP16, and GN01, respectively (Table S4). The median (interquartile range) LSF mass flux (unit: mg/m^2/d) is 229.2 (103.8–403.1) in the GA03, 93.2 (49.2–287.3) in the GP16, and 48.9 (23.4–167.5) in the GN01 (Table S4). We assess the contribution to total mass flux from the LSF size fraction as f_LSF (flux) = $\frac{\text{LSF mass flux}}{\text{TOT mass flux}}$. Median (interquartile range) f_LSF (flux) at all stations throughout the water column is 95.4% (93.0–96.7), 95.9% (94.4–97.0), and 94.6% (92.1–96.8) in the GA03, GP16, and GN01, respectively (Figure 5). Clearly, the contribution to TOT mass flux from particles in the LSF is much more important than from particles in the SSF. This is despite the much smaller contribution of

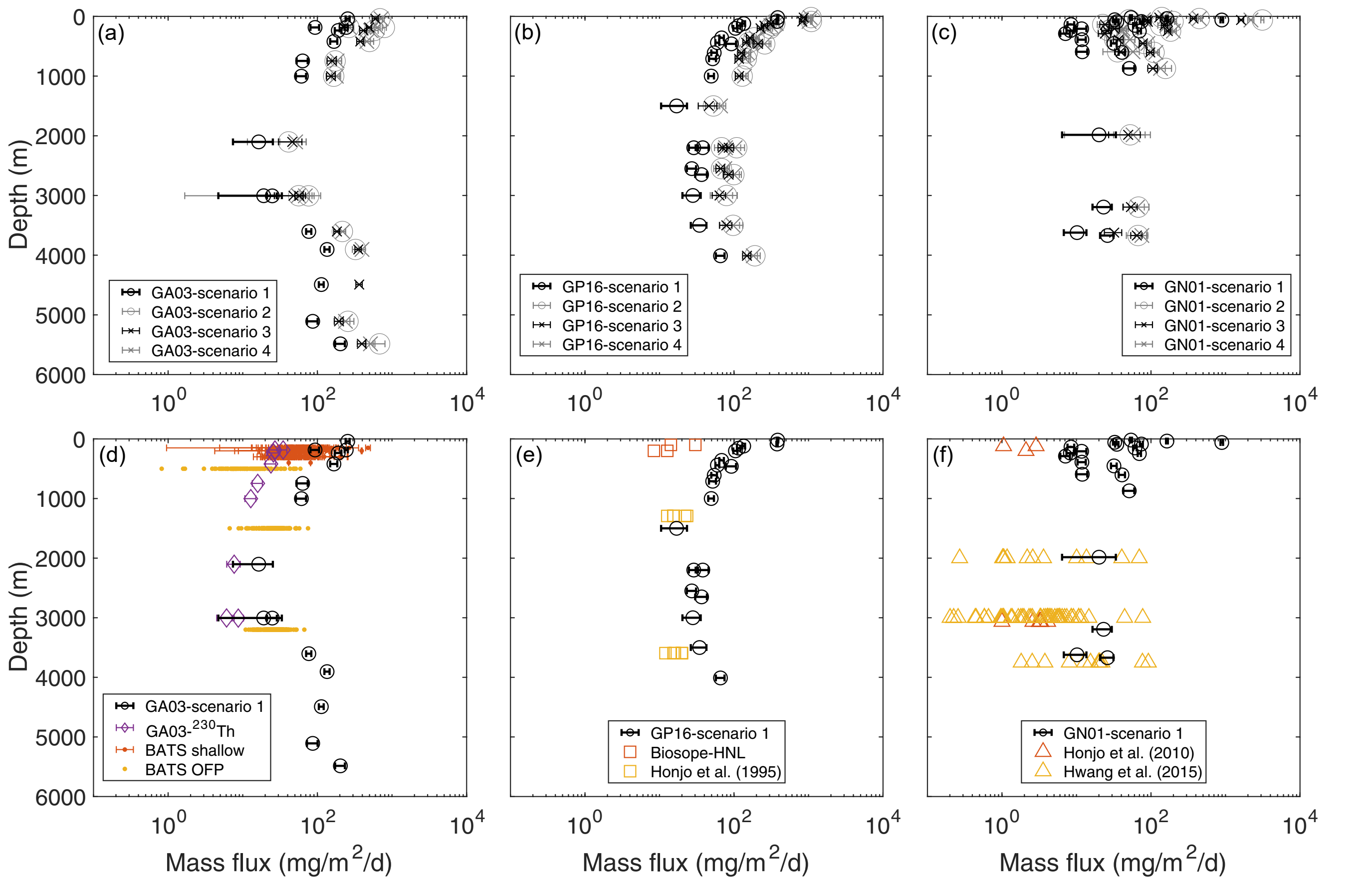

Figure 6. Sensitivity tests of TOT mass flux porosity-size relationships (A&G88 and X22) and upper size limits (2 and 10 mm) for LSF (a–c), and comparisons between pump-derived and ^{230}Th-derived TOT mass flux in GA03 (d), and between pump-derived and sediment trap-measured TOT mass flux (unit: mg/m^2/d) in the three cruises (d–f). Sensitivity scenarios are: (a) X22, 2 mm (small black circles); (b) X22, 10 mm (large gray circles); (c) A&G88, 2 mm (small black x); (d) A&G88, 10 mm (large gray x). The ^{230}Th-derived TOT mass fluxes in (d) are from Stations 10 and 12 in leg 2 of the GA03 cruise, estimated as the product of ^{230}Th flux and SSF SPM/^{230}Th ratio (Hayes, Black, et al., 2018). Only ^{230}Th samples at depth 1,000 m above the seafloor are used due to potential influences from benthic processes. Sediment trap locations and references as for Figure 1. Errors bars are reported as one standard deviation.

LSF particles to total SPM concentrations. Indeed, *f*_LSF (conc), the analogous index to assess the contribution to total SPM from the LSF size fraction, are 23.6% (19.1–29.7), 21.5% (17.3–27.2), and 16.0% (10.6–22.1) in the GA03, GP16, and GN01, respectively (Figure 5). Flux is integrated across sizes, and the faster sinking speed of the LSF is more important than the larger mass concentration of the SSF such that the LSF dominates the TOT flux. Given that the calculation of SSF and LSF sinking velocity uses the same g/η and similar particle densities (LSF to SSF density ratio median: 1.04; interquartile range: 0.94–1.14), it is the difference in particle size and thus WSV*s* between the LSF and SSF that accounts for the large disparity between *f*_LSF (conc) and *f*_LSF (flux).

5. Discussion

5.1. Sensitivity of Mass Flux to Porosity-Size Relationship and Upper Size Limit

The pump-derived mass flux is sensitive to the choice of porosity-size relationship and to the upper size limit i.e., assumed for the LSF. We consider the sensitivity of mass flux calculations in four scenarios: (a) the reference calculation, with an upper size limit of 2 mm and the X22 porosity-size relationship; (b) X22 but with upper size limit of 10 mm; (c) the A&G88 porosity-size relationship, with upper size limit of 2 mm; and (d) A&G88 with upper size limit of 10 mm. Larger particles lead to higher mass flux. Increasing the upper size limit from 2 mm (scenario 1) to 10 mm (scenario 2) leads to an increase in the WSV*s* and thus TOT mass flux of a median (interquartile range) over the three cruises of 187.2% (162.8%–212.7%) (Figures 6a–6c). Keeping an upper size

10.1029/2021GB007292

limit of 2 mm, but changing to the A&G88 porosity-size relationship (scenario 3) also increases WSV*s* and thus TOT mass flux (Figures 6a–6c), with a median (interquartile range) percent increase of 125.7% (109.9%–142.7%) over the three cruises. This is because the A&G88 relationship predicts lower porosities for aggregates <1.4 mm (Figure 2). The relatively small upper limit of 2 mm means that most particles have lower porosities (and thus higher sinking rates) in this scenario. Interestingly, there is almost no sensitivity of the calculated TOT mass flux to changing the porosity-size relationship when the upper size limit 10 mm is used: changing from scenario 2 to 4 leads to a median (interquartile range) percent of increase of only −0.4% (−15.0% to 9.5%) (Figures 6a–6c). This is because the A&G88 relationship results in higher porosities for aggregates >1.4 mm, so the influence of considering very large aggregates, which would otherwise increase mass flux, is reduced because of their higher porosities. These sensitivity tests show that scenarios 2–4 are quite similar and are all higher than our reference scenario 1. Despite scenario 1 being low compared to the others, we show in the next section that it is nonetheless closest to independent observations of mass flux.

5.2. Comparisons of Mass Flux and Sinking Velocities to Other Measurements

5.2.1. Mass Flux Comparisons

Most existing observations of mass fluxes are from sediment traps. Radionuclide-derived estimates of mass flux are less common, but the principle for estimating mass fluxes is the same as for the commonly reported radionuclide-derived POC fluxes (e.g., Hayes, Black, et al., 2018). Here we compare our Stokes' Law-based estimates of mass flux with nearby sediment trap for each of the three cruises and ^{230}Th-based estimates of mass flux at BATS in the GA03 cruise.

We extracted all available sediment trap mass flux measurements from nearby locations from the same season (Conte, 2019; Honjo et al., 1995, 2010; Hwang et al., 2015; Miquel et al., 2006). Our Stokes' Law-based, pump-derived TOT mass fluxes from the reference calculation are comparable to sediment-trap-measured mass fluxes in the deep ocean but are generally about an order of magnitude higher at the surface, especially for GP16 and GN01 (Figures 6d–6f). Pump-derived TOT mass fluxes at the surface in GA03 are on the higher end but overlap with BATS time-series sediment trap fluxes between 1988 and 2016, which exhibit high interannual variabilities (Figure 6d). The difference between measured trap fluxes and pump-derived TOT mass flux in the GP16 and GN01 could be less pronounced if there were also multiple years of sediment trap data in those regions.

We also compared our Stokes' Law-based, pump-derived mass flux with ^{230}Th-derived mass flux at BATS calculated using ^{230}Th production due to uranium decay in the water column and the SPM to particulate ^{230}Th ratio of SSF particles from in-situ pumps, similar to the estimate of ^{230}Th-derived elemental fluxes (Hayes, Black, et al., 2018). Like with the sediment traps, our estimated TOT mass flux from the Stokes' Law-based reference scenario at BATS is higher at the surface and similar in the deep (≥2,000 m) when compared to ^{230}Th-derived TOT mass flux (Figure 6d).

The higher Stokes-based compared to sediment-trap and ^{230}Th-based mass flux in surface waters may be caused by one or more of the following: (a) an overestimation of mass flux derived from pumps, (b) an underestimation by sediment traps or (c) the ^{230}Th method, and/or (d) a mismatch in timescales of integration. We examine these below.

First, an overestimation of mass flux derived from pumps suggests that Stokes' Law-based estimates of weighted sinking velocities (WSV*s*) may be too high. The use of the X22 porosity-size relationship and a relatively small (2 mm) upper size limit compared to the more traditional A&G88 relationship and higher (10 mm) upper size limit already results in lower calculated Stokes-based mass flux in our reference calculation (Figures 6a–6c). Lowering the upper particle size limit even further may be justifiable for some oligotrophic stations, including those used in the comparisons to other methods in Figure 6, but may be unrealistic for more productive stations. The X22 porosity-size relationship predicts higher porosities for smaller aggregates compared to the A&G88 relationship but is heavily weighted by observations from a single mesocosm study (Bach et al., 2016). Aggregates from the Lam and Bishop (2007) data set generally have higher porosities (lower 1-P) than those from the Bach et al. (2016) data set (Figure 2), so it could be that even the X22 relationship underestimates porosities of smaller aggregates. An overestimation of WSV*s* could also result if the real particle mass-size distribution is skewed to even lower particle sizes than suggested by a single power law fit to measured SSF and LSF SPM data (Section 3.3). Other reasons for an overestimate of calculated Stokes-based flux could be: a systematic overestimate of particle density, such as would occur if dense particle phases were actually skewed to smaller particles rather than evenly distributed through size bins (Section 3.2.2); the assumption of spherical particles, which have less drag than other shapes (Section 3.2.4); or by neglecting the influence of TEP (see Section 3.2.4).

Second, it is known that sediment traps can undercollect sinking particles at shallow depths where currents are strong, when particles are slowly sinking (Gustafsson et al., 2004), and when their design uses conical funnels (Baker et al., 2020). Honjo et al. (2010)'s surface-tethered traps in the Western Arctic Ocean (Figure 6f), for example, are conical traps and may undercollect sinking particles. Bottom-tethered conical traps deployed at depth shallower than 1000 m, as for the anchored 500-m Oceanic Flux Program (OFP) trap at BATS, could "undertrap" by a factor of 2 (Yu et al., 2001).

Third, the conversion of ^{230}Th flux to mass flux depends on the SPM/^{230}Th ratios used (cf., Hayes, Black, et al., 2018). Since no LSF ^{230}Th data were measured at BATS, we estimated the ^{230}Th-derived TOT mass flux by multiplying ^{230}Th flux by SSF SPM/^{230}Th. For other stations from the GA03 cruise where both SSF and LSF ^{230}Th were measured ($n = 13$; depth ≥ 966 m), using the LSF SPM/^{230}Th ratio could lead to about two times higher values of TOT mass flux than using SSF SPM/^{230}Th for some samples (Figure S4 in Supporting Information S1). Higher LSF SPM/^{230}Th than SSF SPM/^{230}Th ratios might be expected given that SPM scales with volume whereas adsorption of ^{230}Th scales with surface area, and LSF particles should have a higher volume to surface area ratio. However, using a 2-fold higher LSF SPM/^{230}Th ratio alone would not reconcile the flux estimates. It is also possible that ^{230}Th-based fluxes themselves are more sensitive to the sinking fluxes of small rather than large particles: over the entire GA03 transect, mass fluxes estimated from the ^{230}Th method using SSF SPM/^{230}Th ratios fall between Stokes-based SSF and TOT mass flux, and is more similar to that of the SSF mass flux (Figure S5 in Supporting Information S1). Mass flux and WSV*s* in our method are both mass-based and derived from the particle volume (Equations 10–13), which gives more importance to larger particles and thus a higher TOT mass flux compared to the ^{230}Th method.

Fourth, fluxes estimated from sediment traps, Stokes' Law-based calculations of particles collected by large-volume in-situ pumps, and radionuclide mass-balance techniques integrate over different temporal and spatial scales. Moored sediment traps are usually deployed for weeks and months, neutrally buoyant or surface-drifting traps are deployed for days, whereas pumps collect particles for several hours. It is generally thought that the longer sediment trap deployment times allow them to capture rare, fast-sinking particles better than pumps, but this would not explain the bias to higher mass fluxes from pump particles. If the fluxes estimated from sediment traps and pump particles primarily reflect the sinking of large particles, whose WSV*s* are around 60 m/d (Section 4.1), then the residence time of large particles in a 4,000 m water column is of order 2 months. In contrast, the ^{230}Th flux is an average flux that reflects the timescale of all particles sinking through the water column (3–5 years in the upper ~500 m to 10–20 years in the deep, >2000 m; Hayes, Anderson et al., 2018, Hayes, Black et al., 2018). If timescale were to explain the discrepancy with Stokes' Law-derived mass flux, this would suggest that the particle flux at the time of GA03 sampling was higher than the annual-to-decadal particle flux average. Indeed, ^{230}Th-based POC fluxes from the GA03 occupation of BATS agreed very well with averaged annual (2003–2005 deployments) deep fluxes from the OFP site (Hayes, Black, et al., 2018; Huang & Conte, 2009), suggesting an important timescale component to the mismatch to the Stokes' Law-based calculations with in-situ filtered pump particles.

Regardless of the source of the discrepancies, it is reassuring to observe comparable flux estimates in the deep ocean from all three techniques. The identification of the most important source of the higher flux estimated by the Stokes' Law-based method for shallower samples requires further investigation. The enhancement of flux close to the seafloor estimated from measured particle mass concentrations, such as this study, should be interpreted as a potential sinking flux, since sediment resuspension processes are an additional force that help keep particles aloft.

5.2.2. Sinking Velocity Comparisons

Existing measurements of sinking velocities of natural marine particles, direct or indirect, vary by several orders of magnitude, ranging from several meters to thousands of meters per day (e.g., Alldredge & Gotschalk, 1988; Armstrong et al., 2009; Berelson, 2001; Briggs et al., 2020; Estapa et al., 2019; McDonnell & Buesseler, 2012; Riley et al., 2012; Trull et al., 2008). Our LSF WSV*s* in the upper 500 m at Stations 10 and 12 in leg 2 of the GA03 cruise, ranging from 22.6 to 78.7 m/d, are on the high end but overlap with estimates of 5.9–54.1 m/d measured using gel traps and in situ camera system for particles between 73 and 1,400 μm at BATS at the end of

September in 2009 (McDonnell & Buesseler, 2012). The TOT WSV*s*, however, are almost an order of magnitude higher than 2–3 m/d estimated using a thorium (Th) based inverse method in the same GA03 cruise in the North Atlantic (Lerner et al., 2017). Approximations of the sinking velocity derived from ^{230}Th observations are also about 1–3 m/d in other parts of the ocean (Bacon & Anderson, 1982; Krishnaswami et al., 1981; Rutgers van der Loeff & Berger, 1993; Scholten et al., 1995). In general, the SSF WSV*s* in the three cruises, with the median (interquartile range) of 0.8 (0.6–1.1) m/d (Table S4), are more similar to the values estimated from these Th-based estimates. Burd et al. (2007) pointed out that bulk measurements such as particulate ^{234}Th are likely to represent the properties of small particles more than large particles due to the nature of the Th scavenging process. As discussed in Section 5.2.1, Th-based mass flux and sinking velocity may be weighted to small particles that have higher surface area to volume ratios, and therefore, potentially results in a lower TOT sinking velocity than the Stokes-based method which is less influenced by the specific surface area.

Alternative chemical tracers, such as chloropigments, have also been used with inverse models to calculate sinking velocities for different particle size pools. One of the advantages for using chloropigments as a tracer is that they are not surface-adsorbed tracers like Th isotopes and may thus be more representative of TOT particles than SSF particles. Indeed, sinking rate estimates from a recent chloropigments-based inverse method by Wang et al. (2019) using data from in-situ pumps in the Mediterranean Sea are in good agreement with our study. Their modeled sinking velocities are 66.8 ± 68.6 m/d (mean ± s.d.) for large particles (>70 μm), with a range between 7 and 183 m/d, and 1.8 ± 1.9 m/d, for small particles (1–70 μm), ranging between 0.2 and 5 m/d.

5.3. Controls on the Mass Flux and Particle Sinking Velocity in the Three Cruises

The Stokes' Law-based approach used in this work allows us to take advantage of detailed information about particle characteristics (concentration, composition, and size) measured during the three U.S. GEOTRACES cruises to investigate controls on mass flux and sinking velocity. The Stokes' Law model (Equation 2) shows sinking velocity is positively correlated with g/η (hydrographic effects), particle size (size effects), and particle density (composition effects). Gravitational acceleration varies by less than 1% between Arctic and tropical waters, but viscosity is highly temperature-dependent (Millero, 1974). We have neglected potential biological contributions to viscosity such as from the release of mucous materials including TEP (Jenkinson, 1986, 1993; Jenkinson & Biddanda, 1995; Seuront & Vincent, 2008; Seuront et al., 2006, 2007, 2010). The particle mass size distribution was estimated from measurements of SPM in the SSF and LSF (Section 3.3). Here, we use f_LSF, the ratio between LSF and TOT SPM, as an indirect index for size effects. A higher f_LSF indicates higher abundance of large particles.

We plot depth-binned profiles of four direct measurements (g/η, f_LSF, particle density, and SPM concentration) from each of the three cruises and compare them with profiles of WSV*s* and mass flux (Figure 7). Since TOT mass flux is comprised primarily (>90%) of the contribution from the LSF (Figure 5), for simplicity we focus on the LSF measurements and derived variables. The breakdown for all parameters in all size fractions (SSF, LSF, and TOT) is shown in Figure S6 in Supporting Information S1. Further, because of large contrasts between margin and open ocean stations on each cruise (Figure 4), we focus on comparing the particle characteristics and derived sinking velocities and mass fluxes for "gyre" stations from the three cruises. For GA03 and GP16, we use biogeochemical province definitions of Longhurst (2007) and Black et al. (2020) to define low-latitude gyre stations: Stations 11–12 in leg 1 and Stations 8–24 in leg 2 for GA03; Stations 7–36 for GP16. The gyre stations in the GN01 are defined as stations with bottom depth more than 1,000 m, which includes Stations 14–57.

Of the three cruises, the lowest LSF particle density was found in GA03 due to a high fraction of POM in the LSF (Lam et al., 2015) (Figure 7c). Notably, the consistently lower LSF particle density in the upper 4,000 m of the GA03 generally does not translate to particularly slow WSV*s* due to relatively high abundance of large particles (high f_LSF) and low viscosity (high g/η) waters. Similarly, GN01 LSF particles have relatively high density, but this does not translate to higher LSF WSV due to low abundance of large particles (low f_LSF).

The overall profile shapes of LSF SPM and mass flux are generally similar in all three cruises (Figures 7e and 7f), characterized by a surface maximum that rapidly decreases to a "clear-water minimum" around 2,000–3,000 m, and an increase toward the bottom. Because the vertical profile shapes of mass flux are more similar to SPM than to WSV profiles, SPM concentrations exert first order control on the vertical variation of mass flux, with WSV*s* adding some variability (Figure 7d). Our work, therefore, suggests that particle density plays a less important role

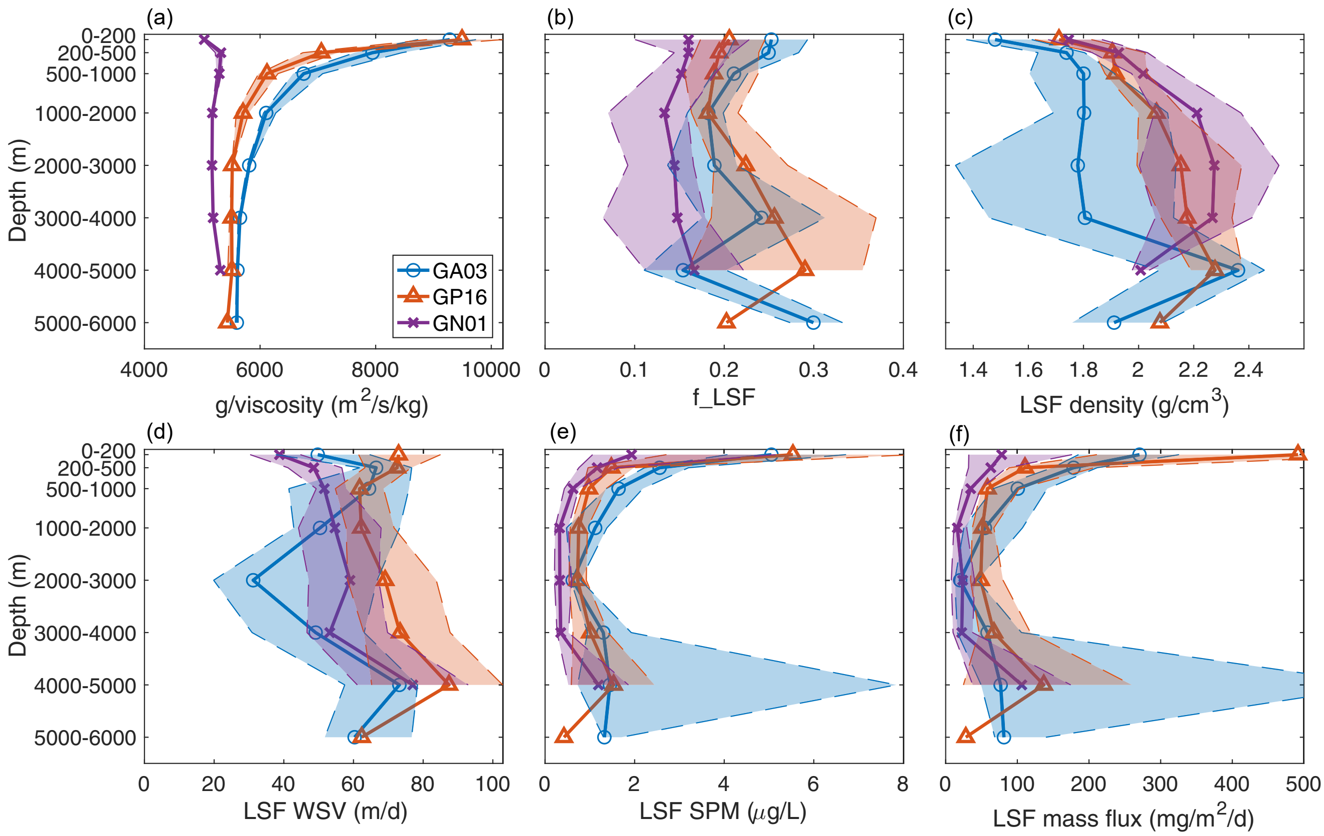

Figure 7. Depth-binned profiles of Stokes-Law-associated parameters and estimated LSF sinking velocity and mass flux in gyre stations in the three cruises. (a): g/η (unit: $m^2/s/kg$); (b): *f*_LSF; (c): LSF density (unit: g/cm^3); (d): LSF WSV (unit: m/d); (e): LSF SPM (unit: μg/L); (f): LSF mass flux (unit: $mg/m^2/d$). The solid line is the median of each depth bin for each cruise, and colored shades within dashed lines are interquartile ranges. The median of each parameter demonstrates the typical profile in the three cruises, and interquartile range reflects the variability.

in controlling the magnitude of WSV*s* than particle size distribution, and WSV*s* play a less important role than SPM in controlling variations of mass flux with depth.

Two interesting features appear in the profiles of LSF mass flux that merit further explanation that we will address in the following sections: (a) why is the GN01 cruise in the Western Arctic Ocean generally characterized by the lowest mass flux? (b) why do particles in the low-latitude North Atlantic (GA03 cruise) have a smaller attenuation in LSF mass flux in the mesopelagic when compared to particles in the low-latitude ETSP (GP16 cruise)?

5.3.1. Low Mass Flux in GN01 in the Western Arctic Ocean

LSF mass flux in GN01 is the lowest among the three cruises (Figures 4d and 7f) as a result of both slow sinking velocity and low mass concentration. The profile of g/η in the Western Arctic Ocean is very different than in the low-latitude oceans. In GN01, g/η is lowest in the surface (~5,000 $m^2/s/kg$), increases to a maximum at about 300 m (~5,400 $m^2/s/kg$), which is slightly below the Pacific-derived halocline, and remains relatively constant below 1,000 m in the deep ocean (~5,200 $m^2/s/kg$) (Figure 7a). In contrast, g/η is highest in the surface waters of GA03 and GP16 (~10,000 $m^2/s/kg$), decreases rapidly with depth because of the large temperature gradient, and remains relatively constant below ~2,000 m. When comparing values of g/η between the three cruises, they differ by <10% in the deep ocean, but can be up to 200% different in the upper water column (Figure 7a). Since WSV*s* are linearly related to g/η, the highly viscous surface Arctic Ocean waters can lead to up to two times smaller WSV*s* in the upper water column than low-latitude oceans, and slightly smaller WSV*s* in the deep ocean.

The abundance of large particles (*f*_LSF) is systematically lower in GN01 than in GA03 and GP16 throughout the water column (Figure 7b), further decreasing WSV*s* in the Western Arctic Ocean. Interestingly, LSF particle density in GN01 is similar to or higher than in GA03 and GP16 (Figure 7c). From this we can infer that it is not the lack of ballast minerals in particles in the Western Arctic Ocean that is responsible for the low particles fluxes there, as Honjo et al. (2010) previously postulated based on two ice-tethered sediment traps. Instead, LSF mass fluxes are especially low in the Arctic because of the relatively slow sinking velocities due to cold, viscous waters (lowest g/η) and a small particle size distribution (lowest f_LSF), combined with the lowest LSF SPM concentrations (Figures 7e and 7f). This conclusion also holds true for the SSF and TOT particles (Figure S6 in Supporting Information S1).

5.3.2. Low Mass Flux Attenuation in GA03 in the North Atlantic Ocean

There appears to be a lower attenuation (higher transfer efficiency) of LSF mass flux from the surface to 1,000 m in the GA03 gyre than in the GP16 gyre: upper 200 m LSF mass flux in GA03 starts off lower than in GP16, but is higher than GP16 between 200 and 1,000 m (Figures 4a, 4b and 7f). A higher transfer efficiency can be explained by faster sinking rates or slower remineralization/dissolution rates. Interestingly, the calculated LSF WSV*s* are similar or slower in GA03 than in GP16 (Figure 7d), and the higher mesopelagic fluxes derive from the higher mesopelagic LSF SPM. These observations suggests that GA03 gyre particles have slower remineralization/dissolution rates than GP16 gyre particles. Note that this comparison excludes the coastal oxygen deficient zone stations in the GP16, where this and previous work (Black et al., 2018; Pavia et al., 2019) have noted high transfer efficiency in the mesopelagic.

In a modeling study, Cram et al. (2018) demonstrated that the attenuation of particle flux globally could be largely explained by the effect of temperature on remineralization rate and of particle size on sinking velocity. Given the similar temperatures and sinking velocities but contrasting transfer efficiencies between the GA03 and GP16 cruises, however, other factors may control remineralization rate. Such factors could relate to differences in the organic and inorganic composition of particles, or colonization of particles by microbial heterotrophs with the appropriate metabolic capability that may make the GA03 particles more functionally recalcitrant (cf., Zakem et al., 2021). For example, LSF particles in the GA03 gyre are characterized by higher fractions of lithogenic particles and lower fractions of $CaCO_3$ and biogenic opal when compared to the GP16 gyre. The effects of different fractions of lithogenic, $CaCO_3$ and opal on the degradation of bulk particles may manifest in two aspects. First, organic matter exported in regions with higher opal and diatoms has been hypothesized to be more labile and loosely packaged, thus leading to more rapid organic matter attenuation (Francois et al., 2002; Henson, Lampitt et al., 2012, Henson, Sanders et al., 2012; Lam et al., 2011; Lima et al., 2014). Indeed, the POC concentrations in GP16 gyre stations attenuate more quickly through the upper 1,000 m than in GA03 gyre stations (Figure S7 in Supporting Information S1). Second, the remineralization length scale for lithogenic particles is longer (less rapid attenuation with depth in upper 1,000 m) than that for $CaCO_3$, both of which are longer than opal (Figure S7 in Supporting Information S1) (Buesseler et al., 2007; Lamborg et al., 2008; Lima et al., 2014). Therefore, not only is the organic matter lability of GA03 particles lower, but the mineral components of GA03 particles are less susceptible to dissolution.

Higher mass flux transfer efficiencies are also observed for SSF particles in the GA03 gyre compared to the GP16 gyre. Here, both higher SSF WSV*s* in GA03 and higher SSF SPM contribute to higher mass flux transfer efficiencies (Figure S6 in Supporting Information S1).

Estimates of remineralization rates (e.g., RESPIRE trap; Boyd et al., 2015), microbial community structure, and zooplankton feeding rates combined with particle composition data are needed to shed light on the potential influence of particle composition on degradation rates more broadly.

6. Conclusions

This work estimates particle mass flux and weighted particle sinking velocities from measurements of size-fractionated particle concentrations and compositions. We use a modified Stokes' law that incorporates a new porosity-size power-law relationship, measured particle composition, and estimates of mass-size distribution for each sample constrained by measured size-fractionated particle mass concentrations to calculate sinking velocity and mass flux. The new porosity-size relationship compiled in this study (X22) leads to estimates of mass flux that are closer to independent measures of mass flux than estimates using the classic Alldredge and Gotschalk (1988) relationship, but still too high in the upper 1,000 m. The new X22 relationship is heavily weighted by the smaller aggregates from a single mesocosm study in a Norwegian fjord. Porosity data for aggregates in the 50 μm-1 mm range from more varied locations are needed to better constrain the overall porosity-size relationship, which could result in multiple power functions or a more complicated non-linear relationship.

We find that the concentration of particles is generally more important than sinking velocities in determining the vertical profile of mass flux. Further, although particle density is clearly an important variable in the calculation of particle sinking speed, it was rarely the controlling variable for determining WSV*s* and thereby mass flux in this data set. Indeed, we did not find support for the hypothesis proposed by Honjo et al. (2010) that a lack of ballast minerals in the Western Arctic Ocean is responsible for low mass fluxes. Instead, the lowest mass fluxes found in the GN01 cruise in the Western Arctic Ocean result from small particle sizes, low particle concentrations, and viscous water.

The particle size distribution is a parameter measured by optical methods that is increasingly used to study the BCP in various cruises and autonomous platforms (Picheral et al., 2017), including the *Tara* Ocean expedition (Guidi et al., 2016), and has the advantage of high spatial and vertical resolution. The conversion from particle size to flux, however, often lacks any direct or indirect information about particle composition (Giering et al., 2020; Stemmann & Boss, 2012). The poor constraints in particle densities were previously noted in Guidi et al. (2016) and might partly explain the discrepancy between sediment trap-measured and UVP-derived mass fluxes (Fender et al., 2019; Guidi et al., 2008). Our approach here has the advantage that we have direct measurements of particle composition, but we need a better constraint on the upper limit of particle size, which optical devices can provide. The mass-size spectra estimated from size-fractionated particles may also help measurements from optical devices to better constrain the fractal dimension of marine particles. However, caution must be taken when using a single power-law size spectrum over a large range of particle sizes because derivations of such distributions assume steady-state conditions and the presence of only a single coagulation process such as fluid shear or differential sedimentation (Burd & Jackson, 2002; Friedlander, 2000). Pairing optical devices such as the UVP with geochemical measurements will help both approaches, which is beneficial to a more holistic understanding of the BCP on a global scale.

Data Availability Statement

All size-fractionated particle concentration and composition data described above are available on the Biological and Chemical Oceanography Data Management Office website (GA03: https://www.bco-dmo.org/dataset/3871; GP16: https://www.bco-dmo.org/dataset/668083; GN01: https://www.bco-dmo.org/dataset/807340). The MATLAB code to estimate mass flux and average sinking rates can be found at https://doi.org/10.5281/zenodo.6426352.

Acknowledgments
This work was supported by NSFOCE-1535854 to PJL. We would like to thank all chief scientists and everyone on board in the GA03, GP16, and GN01 U.S. GEOTRACES cruises. Special thanks to all people in the pump group for helping to collect particle samples at sea. We sincerely thank past and current members in the Lam lab for the continuous assistance in both lab work and data analysis, and Thomas Weber for the help in data visualization. Many thanks to Carl Lamborg, Colleen Hansel, and Robert Anderson for insights in the discussion. We thank Anja Engel, Lennart Bach, Morten Iversen, and Emmanuel Laurenceau-Cornec for contributing porosity data. We thank Maureen Conte for providing the OFP sediment trap data. We also thank 2 anonymous reviewers for their suggestions and comments to improve this manuscript.

References

Alldredge, A. L. (1998). The carbon, nitrogen and mass content of marine snow as a function of aggregate size. *Deep Sea Research Part I: Oceanographic Research Papers*, *45*(4), 529–541. https://doi.org/10.1016/S0967-0637(97)00048-4

Alldredge, A. L., & Gotschalk, C. (1988). In situ settling behavior of marine snow. *Limnology & Oceanography*, *33*(3), 339–351. https://doi.org/10.4319/lo.1988.33.3.0339

Alldredge, A. L., Passow, U., & Logan, B. E. (1993). The abundance and significance of a class of large, transparent organic particles in the ocean. *Deep Sea Research Part I: Oceanographic Research Papers*, *40*(6), 1131–1140. https://doi.org/10.1016/0967-0637(93)90129-Q

Alldredge, A. L., & Silver, M. W. (1988). Characteristics, dynamics and significance of marine snow. *Progress in Oceanography*, *20*(1), 41–82. https://doi.org/10.1016/0079-6611(88)90053-5

Andrews, S., Nover, D., & Schladow, S. G. (2010). Using laser diffraction data to obtain accurate particle size distributions: The role of particle composition. *Limnology and Oceanography: Methods*, *8*(10), 507–526. https://doi.org/10.4319/lom.2010.8.507

Armstrong, R. A., Lee, C., Hedges, J. I., Honjo, S., & Wakeham, S. G. (2001). A new, mechanistic model for organic carbon fluxes in the ocean based on the quantitative association of POC with ballast minerals. *Deep Sea Research Part II: Topical Studies in Oceanography*, *49*(1–3), 219–236. https://doi.org/10.1016/S0967-0645(01)00101-1

Armstrong, R. A., Peterson, M. L., Lee, C., & Wakeham, S. G. (2009). Settling velocity spectra and the ballast ratio hypothesis. *Deep Sea Research Part II: Topical Studies in Oceanography*, *56*(18), 1470–1478. https://doi.org/10.1016/j.dsr2.2008.11.032

Aumont, O., Van Hulten, M., Roy-Barman, M., Dutay, J. C., Éthé, C., & Gehlen, M. (2017). Variable reactivity of particulate organic matter in a global ocean biogeochemical model. *Biogeosciences*, *14*(9), 2321–2341. https://doi.org/10.5194/bg-14-2321-2017

Azetsu-Scott, K., & Passow, U. (2004). Ascending marine particles: Significance of transparent exopolymer particles (TEP) in the upper ocean. *Limnology & Oceanography*, *49*(3), 741–748. https://doi.org/10.4319/lo.2004.49.3.0741

Bach, L. T., Boxhammer, T., Larsen, A., Hildebrandt, N., Schulz, K. G., & Riebesell, U. (2016). Influence of plankton community structure on the sinking velocity of marine aggregates. *Global Biogeochemical Cycles*, *30*(8), 1145–1165. https://doi.org/10.1002/2016GB005372

Bacon, M. P., & Anderson, R. F. (1982). Distribution of thorium isotopes between dissolved and particulate forms in the deep sea. *Journal of Geophysical Research*, *87*(C3), 2045–2056. https://doi.org/10.1029/JC087iC03p02045

Baker, C. A., Estapa, M. L., Iversen, M., Lampitt, R., & Buesseler, K. (2020). Are all sediment traps created equal? An intercomparison study of carbon export methodologies at the PAP-SO site. *Progress in Oceanography*, *184*, 102317. https://doi.org/10.1016/j.pocean.2020.102317

Baumann, K. H., & Sprengel, C. (2000). Morphological variations of selected coccolith species in a sediment trap north of the Canary Islands. *Journal of Nannoplankton Research*, *22*(3), 185–193.

Berelson, W. M. (2001). Particle settling rates increase with depth in the ocean. *Deep Sea Research Part II: Topical Studies in Oceanography*, *49*(1–3), 237–251. https://doi.org/10.1016/S0967-0645(01)00102-3

Bishop, J. K. B., Edmond, J. M., Ketten, D. R., Bacon, M. P., & Silker, W. B. (1977). The chemistry, biology, and vertical flux of particulate matter from the upper 400 m of the equatorial Atlantic Ocean. *Deep-Sea Research*, *24*(6), 511–548. https://doi.org/10.1016/0146-6291(77)90526-4

Black, E. E., Buesseler, K. O., Pike, S. M., & Lam, P. J. (2018). 234Th as a tracer of particulate export and remineralization in the southeastern tropical Pacific. *Marine Chemistry*, *201*, 35–50. https://doi.org/10.1016/j.marchem.2017.06.009

Black, E. E., Kienast, S. S., Lemaitre, N., Lam, P. J., Anderson, R. F., Planquette, H., et al. (2020). Ironing out Fe residence time in the dynamic upper ocean. *Global Biogeochemical Cycles*, *34*(9), e2020GB006592. https://doi.org/10.1029/2020GB006592

Boyd, P. W., McDonnell, A., Valdez, J., LeFevre, D., & Gall, M. P. (2015). Respire: An in situ particle interceptor to conduct particle remineralization and microbial dynamics studies in the oceans' Twilight Zone. *Limnology and Oceanography: Methods*, *13*(9), 494–508. https://doi.org/10.1002/lom3.10043

Boyd, P. W., & Trull, T. W. (2007). Understanding the export of biogenic particles in oceanic waters: Is there consensus? *Progress in Oceanography*, *72*(4), 276–312. https://doi.org/10.1016/j.pocean.2006.10.007

Briggs, N., Dall'Olmo, G., & Claustre, H. (2020). Major role of particle fragmentation in regulating biological sequestration of CO_2 by the oceans. *Science*, *367*(6479), 791–793. https://doi.org/10.1126/science.aay1790

Buesseler, K. O., Antia, A. N., Chen, M., Fowler, S. W., Gardner, W. D., Gustafsson, O., et al. (2007). An assessment of the use of sediment traps for estimating upper ocean particle fluxes. *Journal of Marine Research*, *65*(3), 345–416. https://doi.org/10.1357/002224007781567621

Burd, A. B., & Jackson, G. A. (2002). Modeling steady-state particle size spectra. *Environmental science & technology*, *36*(3), 323–327. https://doi.org/10.1021/es010982n

Burd, A. B., Jackson, G. A., & Moran, S. B. (2007). The role of the particle size spectrum in estimating POC fluxes from Th234/U238 disequilibrium. *Deep Sea Research Part I: Oceanographic Research Papers*, *54*(6), 897–918. https://doi.org/10.1016/j.dsr.2007.03.006

Conte, M. H. (2019). *Primary particle flux data (500, 1500, and 3200m depths) of the OFP sediment trap time-series in the northern Sargasso Sea. Biological and Chemical Oceanography Data Management Office (BCO-DMO), Dataset version 2019-12-13*. http://lod.bco-dmo.org/id/dataset/704722

Cram, J. A., Weber, T., Leung, S. W., McDonnell, A. M. P., Liang, J. H., & Deutsch, C. (2018). The role of particle size, ballast, temperature, and oxygen in the sinking flux to the deep sea. *Global Biogeochemical Cycles*, *32*(5), 858–876. https://doi.org/10.1029/2017GB005710

Cui, X., Lamborg, C. H., Hammerschmidt, C. R., Xiang, Y., & Lam, P. J. (2021). The effect of particle composition and concentration on the partitioning coefficient for mercury in three ocean basins. *Frontiers in Environmental Chemistry*, *2*(6). https://doi.org/10.3389/fenvc.2021.660267

Cutter, G., Kadko, D., & Landing, W. M. (2019). Bottle data from the CTD-ODF carousel on the GEOTRACES Arctic section cruise (HLY1502) from August to October 2015 (U.S. GEOTRACES arctic project). *Biological and chemical Oceanography data management Office (BCO-DMO), dataset version 2019-07-29*. https://doi.org/10.1575/1912/bco-dmo.646825.4

Durkin, C. A., Estapa, M. L., & Buesseler, K. O. (2015). Observations of carbon export by small sinking particles in the upper mesopelagic. *Marine Chemistry*, *175*, 72–81. https://doi.org/10.1016/j.marchem.2015.02.011

Ebersbach, F., & Trull, T. W. (2008). Sinking particle properties from polyacrylamide gels during the KErguelen Ocean and Plateau compared Study (KEOPS): Zooplankton control of carbon export in an area of persistent natural iron inputs in the Southern Ocean. *Limnology & Oceanography*, *53*(1), 212–224. https://doi.org/10.4319/lo.2008.53.1.0212

Engel, A., Szlosek, J., Abramson, L., Liu, Z., & Lee, C. (2009). Investigating the effect of ballasting by $CaCO_3$ in Emiliania huxleyi: I. Formation, settling velocities and physical properties of aggregates. *Deep Sea Research Part II: Topical Studies in Oceanography*, *56*(18), 1396–1407. https://doi.org/10.1016/j.dsr2.2008.11.027

Estapa, M. L., Feen, M. L., & Breves, E. (2019). Direct observations of biological carbon export from profiling floats in the subtropical North Atlantic. *Global Biogeochemical Cycles*, *33*(3), 282–300. https://doi.org/10.1029/2018gb006098

Fender, C. K., Kelly, T. B., Guidi, L., Ohman, M. D., Smith, M. C., & Stukel, M. R. (2019). Investigating particle size-flux relationships and the biological pump across a range of plankton ecosystem states from coastal to oligotrophic. *Frontiers in Marine Science*, *6*(603). https://doi.org/10.3389/fmars.2019.00603

Fowler, S. W., & Knauer, G. A. (1986). Role of large particles in the transport of elements and organic compounds through the oceanic water column. *Progress in Oceanography*, *16*(3), 147–194. https://doi.org/10.1016/0079-6611(86)90032-7

Francois, R., Honjo, S., Krishfield, R., & Manganini, S. (2002). Factors controlling the flux of organic carbon to the bathypelagic zone of the ocean. *Global Biogeochemical Cycles*, *16*(4), 34-1–34-20. https://doi.org/10.1029/2001gb001722

Friedlander, S. K. (2000). *Smoke, dust, and haze: Fundamentals of aerosol dynamics* (2nd ed.). Oxford University Press.

Giering, S. L. C., Cavan, E. L., Basedow, S. L., Briggs, N., Burd, A. B., Darroch, L. J., et al. (2020). Sinking organic particles in the ocean- flux estimates from in situ optical devices. *Frontiers in Marine Science*, *6*(834). https://doi.org/10.3389/fmars.2019.00834

Green, R. E., Sosik, H. M., & Olson, R. J. (2003a). Contributions of phytoplankton and other particles to inherent optical properties in New England continental shelf waters. *Limnology & Oceanography*, *48*(6), 2377–2391. https://doi.org/10.4319/lo.2003.48.6.2377

Green, R. E., Sosik, H. M., Olson, R. J., & DuRand, M. D. (2003b). Flow cytometric determination of size and complex refractive index for marine particles: Comparison with independent and bulk estimates. *Applied Optics*, *42*(3), 526–541. https://doi.org/10.1364/AO.42.000526

Guidi, L., Chaffron, S., Bittner, L., Eveillard, D., Larhlimi, A., Roux, S., et al. (2016). Plankton networks driving carbon export in the oligotrophic ocean. *Nature*, *532*(7600), 465–470. https://doi.org/10.1038/nature16942

Guidi, L., Jackson, G. A., Stemmann, L., Miquel, J. C., Picheral, M., & Gorsky, G. (2008). Relationship between particle size distribution and flux in the mesopelagic zone. *Deep Sea Research Part I: Oceanographic Research Papers*, *55*(10), 1364–1374. https://doi.org/10.1016/j.dsr.2008.05.014

Gustafsson, Ö., Andersson, P., Roos, P., Kukulska, Z., Broman, D., Larsson, U., et al. (2004). Evaluation of the collection efficiency of upper ocean sub-photic-layer sediment traps: A 24-month in situ calibration in the open Baltic sea using 234Th. *Limnology and Oceanography: Methods*, *2*(2), 62–74. https://doi.org/10.4319/lom.2004.2.62

Hayes, C. T., Anderson, R. F., Cheng, H., Conway, T. M., Edwards, R. L., Fleisher, M. Q., et al. (2018a). Replacement times of a spectrum of elements in the North Atlantic based on thorium supply. *Global Biogeochemical Cycles*, *32*(9), 1294–1311. https://doi.org/10.1029/2017GB005839

Hayes, C. T., Black, E. E., Anderson, R. F., Baskaran, M., Buesseler, K. O., Charette, M. A., et al. (2018b). Flux of particulate elements in the North Atlantic Ocean constrained by multiple radionuclides. *Global Biogeochemical Cycles*, *32*(12), 1738–1758. https://doi.org/10.1029/2018GB005994

Henson, S., Lampitt, R., & Johns, D. (2012a). Variability in phytoplankton community structure in response to the North Atlantic Oscillation and implications for organic carbon flux. *Limnology & Oceanography*, *57*(6), 1591–1601. https://doi.org/10.4319/lo.2012.57.6.1591

Henson, S. A., Sanders, R., & Madsen, E. (2012b). Global patterns in efficiency of particulate organic carbon export and transfer to the deep ocean. *Global Biogeochemical Cycles*, *26*(1). https://doi.org/10.1029/2011GB004099

Honjo, S., Dymond, J., Collier, R., & Manganini, S. J. (1995). Export production of particles to the interior of the equatorial Pacific Ocean during the 1992 EqPac experiment. *Deep Sea Research Part II: Topical Studies in Oceanography*, *42*(2–3), 831–870. https://doi.org/10.1016/0967-0645(95)00034-N

Honjo, S., Krishfield, R. A., Eglinton, T. I., Manganini, S. J., Kemp, J. N., Doherty, K., et al. (2010). Biological pump processes in the cryopelagic and hemipelagic Arctic Ocean: Canada basin and Chukchi Rise. *Progress in Oceanography*, *85*(3–4), 137–170. https://doi.org/10.1016/j.pocean.2010.02.009

Honjo, S., Manganini, S. J., Krishfield, R. A., & Francois, R. (2008). Particulate organic carbon fluxes to the Ocean interior and factors controlling the biological pump: A synthesis of global sediment trap programs since 1983. *Progress in Oceanography*, *76*(3), 217–285. https://doi.org/10.1016/j.pocean.2007.11.003

Huang, S., & Conte, M. H. (2009). Source/process apportionment of major and trace elements in sinking particles in the Sargasso Sea. *Geochimica et Cosmochimica Acta*, *73*(1), 65–90. https://doi.org/10.1016/j.gca.2008.08.023

Hurd, D. C., & Theyer, F. (1977). Changes in the physical and chemical properties of biogenic silica from the central equatorial Pacific; Part II, Refractive index, density, and water content of acid-cleaned samples. *American Journal of Science*, *277*(9), 1168–1202. https://doi.org/10.2475/ajs.277.9.1168

Hwang, J., Kim, M., Manganini, S. J., McIntyre, C. P., Haghipour, N., Park, J., et al. (2015). Temporal and spatial variability of particle transport in the deep Arctic Canada Basin. *Journal of Geophysical Research: Oceans*, *120*(4), 2784–2799. https://doi.org/10.1002/2014jc010643

Iversen, M. H., & Ploug, H. (2010). Ballast minerals and the sinking carbon flux in the Ocean: Carbon-specific respiration rates and sinking velocity of marine snow aggregates. *Biogeosciences*, *7*(9), 2613–2624. https://doi.org/10.5194/bg-7-2613-2010

Iversen, M. H., & Robert, M. L. (2015). Ballasting effects of smectite on aggregate formation and export from a natural plankton community. *Marine Chemistry*, *175*, 18–27. https://doi.org/10.1016/j.marchem.2015.04.009

Jackson, G. A. (1990). A model of the formation of marine algal flocs by physical coagulation processes. *Deep-Sea Research Part A. Oceanographic Research Papers*, *37*(8), 1197–1211. https://doi.org/10.1016/0198-0149(90)90038-W

Jackson, G. A., Logan, B. E., Alldredge, A. L., & Dam, H. G. (1995). Combining particle size spectra from a mesocosm experiment measured using photographic and aperture impedance (Coulter and Elzone) techniques. *Deep Sea Research Part II: Topical Studies in Oceanography*, *42*(1), 139–157. https://doi.org/10.1016/0967-0645(95)00009-F

Jackson, G. A., Maffione, R., Costello, D. K., Alldredge, A. L., Logan, B. E., & Dam, H. G. (1997). Particle size spectra between 1 μm and 1 cm at Monterey Bay determined using multiple instruments. *Deep Sea Research Part I: Oceanographic Research Papers*, *44*(11), 1739–1767. https://doi.org/10.1016/S0967-0637(97)00029-0

Jenkinson, I. R. (1986). Oceanographic implications of non-Newtonian properties found in phytoplankton cultures. *Nature*, *323*(6087), 435–437. https://doi.org/10.1038/323435a0

Jenkinson, I. R. (1993). Bulk-phase viscoelastic properties of seawater. *Oceanologica Acta*, *16*(4), 317–334.

Jenkinson, I. R., & Biddanda, B. A. (1995). Bulk-phase viscoelastic properties of seawater relationship with plankton components. *Journal of Plankton Research*, *17*(12), 2251–2274. https://doi.org/10.1093/plankt/17.12.2251

Kilps, J. R., Logan, B. E., & Alldredge, A. L. (1994). Fractal dimensions of marine snow determined from image analysis of in situ photographs. *Deep Sea Research Part I: Oceanographic Research Papers*, *41*(8), 1159–1169. https://doi.org/10.1016/0967-0637(94)90038-8

Kiørboe, T., Ploug, H., & Thygesen, U. H. (2001). Fluid motion and solute distribution around sinking aggregates. I. Small-scale fluxes and heterogeneity of nutrients in the pelagic environment. *Marine Ecology Progress Series*, *211*, 1–13. https://doi.org/10.3354/meps211001

Klaas, C., & Archer, D. E. (2002). Association of sinking organic matter with various types of mineral ballast in the deep sea: Implications for the rain ratio. *Global Biogeochemical Cycles*, *16*(4), 63-1–63-14. https://doi.org/10.1029/2001GB001765

Krishnaswami, S., Sarin, M. M., & Somayajulu, B. L. K. (1981). Chemical and radiochemical investigations of surface and deep particles of the Indian Ocean. *Earth and Planetary Science Letters*, *54*(1), 81–96. https://doi.org/10.1016/0012-821X(81)90071-6

Kwon, E. Y., Primeau, F., & Sarmiento, J. L. (2009). The impact of remineralization depth on the air–sea carbon balance. *Nature Geoscience*, *2*(9), 630–635. https://doi.org/10.1038/ngeo612

Lam, P. J., & Bishop, J. K. B. (2007). High biomass, low export regimes in the Southern Ocean. *Deep Sea Research Part II: Topical Studies in Oceanography*, *54*(5–7), 601–638. https://doi.org/10.1016/j.dsr2.2007.01.013

Lam, P. J., Doney, S. C., & Bishop, J. K. B. (2011). The dynamic ocean biological pump: Insights from a global compilation of particulate organic carbon, $CaCO_3$, and opal concentration profiles from the mesopelagic. *Global Biogeochemical Cycles*, *25*(3). https://doi.org/10.1029/2010gb003868

Lam, P. J., Lee, J. M., Heller, M. I., Mehic, S., Xiang, Y., & Bates, N. R. (2018). Size-fractionated distributions of suspended particle concentration and major phase composition from the US GEOTRACES Eastern Pacific Zonal Transect (GP16). *Marine Chemistry*, *201*, 90–107. https://doi.org/10.1016/j.marchem.2017.08.013

Lam, P. J., & Marchal, O. (2015). Insights into particle cycling from thorium and particle data. *Annual Review of Marine Science*, *7*(1), 159–184. https://doi.org/10.1146/annurev-marine-010814-015623

Lam, P. J., Ohnemus, D. C., & Auro, M. E. (2015). Size-fractionated major particle composition and concentrations from the US GEOTRACES North Atlantic zonal transect. *Deep Sea Research Part II: Topical Studies in Oceanography*, *116*, 303–320. https://doi.org/10.1016/j.dsr2.2014.11.020

Lamborg, C. H., Buesseler, K. O., Valdes, J., Bertrand, C. H., Bidigare, R., Manganini, S., et al. (2008). The flux of bio- and lithogenic material associated with sinking particles in the mesopelagic "twilight zone" of the northwest and North Central Pacific Ocean. *Deep Sea Research Part II: Topical Studies in Oceanography*, *55*(14–15), 1540–1563. https://doi.org/10.1016/j.dsr2.2008.04.011

Laurenceau-Cornec, E. C., Le Moigne, F. A. C., Gallinari, M., Moriceau, B., Toullec, J., Iversen, M. H., et al. (2020). New guidelines for the application of Stokes' models to the sinking velocity of marine aggregates. *Limnology & Oceanography*, *65*(6), 1264–1285. https://doi.org/10.1002/lno.11388

Laurenceau-Cornec, E. C., Trull, T. W., Davies, D. M., Bray, S. G., Doran, J., Planchon, F., et al. (2015a). The relative importance of phytoplankton aggregates and zooplankton fecal pellets to carbon export: Insights from free-drifting sediment trap deployments in naturally iron-fertilised waters near the Kerguelen plateau. *Biogeosciences*, *12*(4), 1007–1027. https://doi.org/10.5194/bg-12-1007-2015

Laurenceau-Cornec, E. C., Trull, T. W., Davies, D. M., Christina, L., & Blain, S. (2015b). Phytoplankton morphology controls on marine snow sinking velocity. *Marine Ecology Progress Series*, *520*, 35–56. https://doi.org/10.3354/meps11116

Lee, C., Peterson, M. L., Wakeham, S. G., Armstrong, R. A., Cochran, J. K., Miquel, J. C., et al. (2009). Particulate organic matter and ballast fluxes measured using time-series and settling velocity sediment traps in the northwestern Mediterranean Sea. *Deep Sea Research Part II: Topical Studies in Oceanography*, *56*(18), 1420–1436. https://doi.org/10.1016/j.dsr2.2008.11.029

Le Moigne, F. A. C., Sanders, R. J., Villa-Alfageme, M., Martin, A. P., Pabortsava, K., Planquette, H., et al. (2012). On the proportion of ballast versus non-ballast associated carbon export in the surface ocean. *Geophysical Research Letters*, *39*(15). https://doi.org/10.1029/2012GL052980

Lerner, P., Marchal, O., Lam, P. J., Buesseler, K., & Charette, M. A. (2017). Kinetics of thorium and particle cycling along the U.S. GEOTRACES North Atlantic transect. *Deep Sea Research Part I: Oceanographic Research Papers*, *125*, 106–128. https://doi.org/10.1016/j.dsr.2017.05.003

Lima, I. D., Lam, P. J., & Doney, S. C. (2014). Dynamics of particulate organic carbon flux in a global ocean model. *Biogeosciences*, *11*(4), 1177–1198. https://doi.org/10.5194/bg-11-1177-2014

Logan, B. E., & Alldredge, A. L. (1989). Potential for increased nutrient uptake by flocculating diatoms. *Marine Biology*, *101*(4), 443–450. https://doi.org/10.1007/BF00541645

Logan, B. E., & Wilkinson, D. B. (1990). Fractal geometry of marine snow and other biological aggregates. *Limnology & Oceanography*, *35*(1), 130–136. https://doi.org/10.4319/lo.1990.35.1.0130

Loisel, H., Nicolas, J. M., Sciandra, A., Stramski, D., & Poteau, A. (2006). Spectral dependency of optical backscattering by marine particles from satellite remote sensing of the global ocean. *Journal of Geophysical Research*, *111*(C9), C09024. https://doi.org/10.1029/2005JC003367

Longhurst, A. R. (2007). Toward an ecological geography of the sea. In A. R. Longhurst (Ed.), *Ecological geography of The sea* (2nd ed., pp. 1–17). Academic Press. https://doi.org/10.1016/B978-012455521-1/50002-4

Martin, J. H., Knauer, G. A., Karl, D. M., & Broenkow, W. W. (1987). Vertex: Carbon cycling in the northeast Pacific. *Deep-Sea Research Part A. Oceanographic Research Papers*, *34*(2), 267–285. https://doi.org/10.1016/0198-0149(87)90086-0

McCave, I. N. (1975). Vertical flux of particles in the ocean. *Deep-Sea Research and Oceanographic Abstracts*, *22*(7), 491–502. https://doi.org/10.1016/0011-7471(75)90022-4

McDonnell, A. M., & Buesseler, K. O. (2010). Variability in the average sinking velocity of marine particles. *Limnology & Oceanography*, *55*(5), 2085–2096. https://doi.org/10.4319/lo.2010.55.5.2085

McDonnell, A. M. P., & Buesseler, K. O. (2012). A new method for the estimation of sinking particle fluxes from measurements of the particle size distribution, average sinking velocity, and carbon content. *Limnology and Oceanography: Methods*, *10*(5), 329–346. https://doi.org/10.4319/lom.2012.10.329

McDougall, T. J., & Barker, P. M. (2011). Getting started with TEOS-10 and the Gibbs Seawater (GSW) oceanographic toolbox. *SCOR/IAPSO, WG127*, 1–28.

Michaels, A. F., & Silver, M. W. (1988). Primary production, sinking fluxes and the microbial food web. *Deep-Sea Research Part A. Oceanographic Research Papers*, *35*(4), 473–490. https://doi.org/10.1016/0198-0149(88)90126-4

Millero, F. J. (1974). Seawater as a multicomponent electrolyte solution. In E. D. Goldberg (Ed.), *The Sea, volume 5: Marine chemistry* (pp. 3–80). John Wiley & Sons Inc.

Miquel, J., Gasser, B., & Claustre, H. (2006). *Export fluxes in contrasting environments of the South-East Pacific Ocean derived from drifting sediment traps (BIOSOPE)*. AGU. Paper presented at AGU Fall Meeting.

Omand, M. M., Govindarajan, R., He, J., & Mahadevan, A. (2020). Sinking flux of particulate organic matter in the oceans: Sensitivity to particle characteristics. *Scientific Reports*, *10*(1), 1–16. https://doi.org/10.1038/s41598-020-60424-5

Passow, U. (2002). Transparent exopolymer particles (TEP) in aquatic environments. *Progress in Oceanography*, *55*(3), 287–333. https://doi.org/10.1016/S0079-6611(02)00138-6

Pavia, F. J., Anderson, R. F., Lam, P. J., Cael, B. B., Vivancos, S. M., Fleisher, M. Q., et al. (2019). Shallow particulate organic carbon regeneration in the South Pacific Ocean. *Proceedings of the National Academy of Sciences*, *116*(20), 9753–9758. https://doi.org/10.1073/pnas.1901863116

Peters, B. D., Lam, P. J., & Casciotti, K. L. (2018). Nitrogen and oxygen isotope measurements of nitrate along the US GEOTRACES Eastern Pacific Zonal Transect (GP16) yield insights into nitrate supply, remineralization, and water mass transport. *Marine Chemistry*, *201*, 137–150. https://doi.org/10.1016/j.marchem.2017.09.009

Picheral, M., Colin, S., & Irisson, J. O. (2017). *EcoTaxa, a tool for the taxonomic classification of images*. http://ecotaxa.obs-vlfr.fr

Ploug, H., Iversen, M. H., & Fischer, G. (2008a). Ballast, sinking velocity, and apparent diffusivity within marine snow and zooplankton fecal pellets: Implications for substrate turnover by attached bacteria. *Limnology & Oceanography*, *53*(5), 1878–1886. https://doi.org/10.4319/lo.2008.53.5.1878

Ploug, H., Iversen, M. H., Koski, M., & Buitenhuis, E. T. (2008b). Production, oxygen respiration rates, and sinking velocity of copepod fecal pellets: Direct measurements of ballasting by opal and calcite. *Limnology & Oceanography*, *53*(2), 469–476. https://doi.org/10.4319/lo.2008.53.2.0469

Ploug, H., & Passow, U. (2007). Direct measurement of diffusivity within diatom aggregates containing transparent exopolymer particles. *Limnology & Oceanography*, *52*(1), 1–6. https://doi.org/10.4319/lo.2007.52.1.0001

Prairie, J. C., Ziervogel, K., Camassa, R., McLaughlin, R. M., White, B. L., Dewald, C., & Arnosti, C. (2015). Delayed settling of marine snow: Effects of density gradient and particle properties and implications for carbon cycling. *Marine Chemistry*, *175*, 28–38. https://doi.org/10.1016/j.marchem.2015.04.006

Puigcorbé, V., Benitez-Nelson, C. R., Masqué, P., Verdeny, E., White, A. E., Popp, B. N., et al. (2015). Small phytoplankton drive high summertime carbon and nutrient export in the Gulf of California and Eastern Tropical North Pacific. *Global Biogeochemical Cycles*, *29*(8), 1309–1332. https://doi.org/10.1002/2015gb005134

Rea, D. K., & Hovan, S. A. (1995). Grain size distribution and depositional processes of the mineral component of abyssal sediments: Lessons from the North Pacific. *Paleoceanography*, *10*(2), 251–258. https://doi.org/10.1029/94PA03355

Reynolds, R. A., Stramski, D., & Neukermans, G. (2016). Optical backscattering by particles in Arctic seawater and relationships to particle mass concentration, size distribution, and bulk composition. *Limnology & Oceanography*, *61*(5), 1869–1890. https://doi.org/10.1002/lno.10341

Riley, J. S., Sanders, R., Marsay, C., Le Moigne, F. A. C., Achterberg, E. P., & Poulton, A. J. (2012). The relative contribution of fast and slow sinking particles to ocean carbon export. *Global Biogeochemical Cycles*, *26*(1). https://doi.org/10.1029/2011gb004085

Rixen, T., Gaye, B., Emeis, K., & Ramaswamy, V. (2019). The ballast effect of lithogenic matter and its influences on the carbon fluxes in the Indian Ocean. *Biogeosciences*, *16*(2), 485–503. https://doi.org/10.5194/bg-16-485-2019

Rohatgi, A. (2010). *WebPlotDigitizer- Extract data from plots, images, and maps*. https://automeris.io/WebPlotDigitizer/

Rosengard, S. Z., Lam, P. J., Balch, W. M., Auro, M. E., Pike, S., Drapeau, D., & Bowler, B. (2015). Carbon export and transfer to depth across the southern ocean Great calcite Belt. *Biogeosciences*, *12*(13), 3953–3971. https://doi.org/10.5194/bg-12-3953-2015

Roullier, F., Berline, L., Guidi, L., Durrieu De Madron, X., Picheral, M., Sciandra, A., et al. (2014). Particle size distribution and estimated carbon flux across the Arabian Sea oxygen minimum zone. *Biogeosciences*, *11*(16), 4541–4557. https://doi.org/10.5194/bg-11-4541-2014

Ruiz, J. (1997). What generates daily cycles of marine snow? *Deep Sea Research Part I: Oceanographic Research Papers*, *44*(7), 1105–1126. https://doi.org/10.1016/S0967-0637(97)00012-5

Rutgers van der Loeff, M. M., & Berger, G. W. (1993). Scavenging of 230Th and 231Pa near the Antarctic polar front in the South Atlantic. *Deep Sea Research Part I: Oceanographic Research Papers*, *40*(2), 339–357. https://doi.org/10.1016/0967-0637(93)90007-P

Schlitzer, R., Anderson, R. F., Dodas, E. M., Lohan, M., Geibert, W., Tagliabue, A., et al. (2018). The GEOTRACES intermediate data product 2017. *Chemical Geology*, *493*(C), 210–223. https://doi.org/10.1016/j.chemgeo.2018.05.040

Schmidt, K., De La Rocha, C. L., Gallinari, M., & Cortese, G. (2014). Not all calcite ballast is created equal: Differing effects of foraminiferan and coccolith calcite on the formation and sinking of aggregates. *Biogeosciences*, *11*(1), 135–145. https://doi.org/10.5194/bg-11-135-2014

Scholten, J. C., Rutgers van der Loeff, M. M., & Michel, A. (1995). Distribution of 230Th and 231Pa in the water column in relation to the ventilation of the deep Arctic basins. *Deep Sea Research Part II: Topical Studies in Oceanography*, *42*(6), 1519–1531. https://doi.org/10.1016/0967-0645(95)00052-6

Seuront, L., Lacheze, C., Doubell, M. J., Seymour, J. R., Van Dongen-Vogels, V., Newton, K., et al. (2007). The influence of Phaeocystis globosa on microscale spatial patterns of chlorophyll a and bulk-phase seawater viscosity. In M. A. van Leeuwe, J. Stefels, S. Belviso, C. Lancelot, P. G. Verity & W. W. C. Gieskes (Eds.), *Phaeocystis, major link in the biogeochemical cycling of climate-relevant elements* (pp. 173–188). Springer Netherlands. https://doi.org/10.1007/978-1-4020-6214-8_13

Seuront, L., Leterme, S. C., Seymour, J. R., Mitchell, J. G., Ashcroft, D., Noble, W., et al. (2010). Role of microbial and phytoplanktonic communities in the control of seawater viscosity off East Antarctica (30-80°E). *Deep Sea Research Part II: Topical Studies in Oceanography*, *57*(9), 877–886. https://doi.org/10.1016/j.dsr2.2008.09.018

Seuront, L., & Vincent, D. (2008). Increased seawater viscosity, Phaeocystis globosa spring bloom and Temora longicornis feeding and swimming behaviours. *Marine Ecology Progress Series*, *363*, 131–145. https://doi.org/10.3354/meps07373

Seuront, L., Vincent, D., & Mitchell, J. G. (2006). Biologically induced modification of seawater viscosity in the Eastern English Channel during a Phaeocystis globosa spring bloom. *Journal of Marine Systems*, *61*(3), 118–133. https://doi.org/10.1016/j.jmarsys.2005.04.010

Shanks, A. L., & Edmondson, E. W. (1989). Laboratory-made artificial marine snow: A biological model of the real thing. *Marine Biology*, *101*(4), 463–470. https://doi.org/10.1007/BF00541648

Smyth, T. J., Tarran, G. A., & Sathyendranath, S. (2019). Marine picoplankton size distribution and optical property contrasts throughout the Atlantic Ocean revealed using flow cytometry. *Applied Optics*, *58*(32), 8802–8815. https://doi.org/10.1364/AO.58.008802

Steinberg, D. K., Carlson, C. A., Bates, N. R., Johnson, R. J., Michaels, A. F., & Knap, A. H. (2001). Overview of the US JGOFS Bermuda atlantic time-series study (BATS): A decade-scale look at ocean biology and biogeochemistry. *Deep Sea Research Part II: Topical Studies in Oceanography*, *48*(8), 1405–1447. https://doi.org/10.1016/S0967-0645(00)00148-X

Stemmann, L., & Boss, E. (2012). Plankton and particle size and packaging: From determining optical properties to driving the biological pump. *Annual Review of Marine Science*, *4*(1), 263–290. https://doi.org/10.1146/annurev-marine-120710-100853

Stemmann, L., Eloire, D., Sciandra, A., Jackson, G. A., Guidi, L., Picheral, M., & Gorsky, G. (2008). Volume distribution for particles between 3.5 to 2000 μm in the upper 200 m region of the South Pacific Gyre. *Biogeosciences*, *5*(2), 299–310. https://doi.org/10.5194/bg-5-299-2008

Stemmann, L., Jackson, G. A., & Ianson, D. (2004). A vertical model of particle size distributions and fluxes in the midwater column that includes biological and physical processes—Part I: Model formulation. *Deep Sea Research Part I: Oceanographic Research Papers*, *51*(7), 865–884. https://doi.org/10.1016/j.dsr.2004.03.001

Stokes, G. G. (1851). On the effect of the internal friction of fluids on the motion of pendulums. *Transactions of the Cambridge Philosophical Society*, *9*, 8–106.

Stramski, D., Bricaud, A., & Morel, A. (2001). Modeling the inherent optical properties of the ocean based on the detailed composition of the planktonic community. *Applied Optics*, *40*(18), 2929–2945. https://doi.org/10.1364/AO.40.002929

Towe, K. M., & Bradley, W. F. (1967). Mineralogical constitution of colloidal “hydrous ferric oxides”. *Journal of Colloid and Interface Science*, *24*(3), 384–392. https://doi.org/10.1016/0021-9797(67)90266-4

Trull, T. W., Bray, S. G., Buesseler, K. O., Lamborg, C. H., Manganini, S., Moy, C., & Valdes, J. (2008). In situ measurement of mesopelagic particle sinking rates and the control of carbon transfer to the ocean interior during the Vertical Flux in the Global Ocean (VERTIGO) voyages in the North Pacific. *Deep Sea Research Part II: Topical Studies in Oceanography*, *55*(14), 1684–1695. https://doi.org/10.1016/j.dsr2.2008.04.021

Turner, J. T. (2015). Zooplankton fecal pellets, marine snow, phytodetritus and the ocean’s biological pump. *Progress in Oceanography*, *130*, 205–248. https://doi.org/10.1016/j.pocean.2014.08.005

Volk, T., & Hoffert, M. I. (1985). Ocean carbon pumps: Analysis of relative strengths and efficiencies in ocean-driven atmospheric CO_2 changes. In E. T. Sundquist & W. S. Broecker (Eds.), *The carbon cycle and atmospheric CO2: Natural variations Archean to present* (Vol. 32, pp. 99–110). American Geophysical Union. https://doi.org/10.1029/GM032p0099

Wang, W. L., Lee, C., & Primeau, F. W. (2019). A Bayesian statistical approach to inferring particle dynamics from in-situ pump POC and chloropigment data from the Mediterranean Sea. *Marine Chemistry*, *214*, 103654. https://doi.org/10.1016/j.marchem.2019.04.006

White, F. M. (1974). *Viscous fluid flow*. McGraw-Hill Inc.

Wilson, S. E., Ruhl, H. A., Smith, J., K. L. (2013). Zooplankton fecal pellet flux in the abyssal northeast Pacific: A 15 year time-series study. *Limnology & Oceanography*, *58*(3), 881–892. https://doi.org/10.4319/lo.2013.58.3.0881

Woźniak, S. B., Stramski, D., Stramska, M., Reynolds, R. A., Wright, V. M., Miksic, E. Y., et al. (2010). Optical variability of seawater in relation to particle concentration, composition, and size distribution in the nearshore marine environment at Imperial Beach, California. *Journal of Geophysical Research*, *115*(C8), C08027. https://doi.org/10.1029/2009jc005554

Xiang, Y., & Lam, P. J. (2020). Size-fractionated compositions of marine suspended particles in the Western Arctic Ocean: Lateral and vertical sources. *Journal of Geophysical Research: Oceans*, *125*(8), e2020JC016144. https://doi.org/10.1029/2020JC016144

Young, J. R. (1994). Functions of coccoliths. In A. Winter & W. G. Siesser (Eds.), *Coccolithophores* (pp. 63–82). Cambridge University Press.

Yu, E. F., Francois, R., Bacon, M. P., Honjo, S., Fleer, A. P., Manganini, S. J., et al. (2001). Trapping efficiency of bottom-tethered sediment traps estimated from the intercepted fluxes of 230Th and 231Pa. *Deep Sea Research Part I: Oceanographic Research Papers*, *48*(3), 865–889. https://doi.org/10.1016/S0967-0637(00)00067-4

Zakem, E. J., Cael, B. B., & Levine, N. M. (2021). A unified theory for organic matter accumulation. *Proceedings of the National Academy of Sciences*, *118*(6), e2016896118. https://doi.org/10.1073/pnas.2016896118

References From the Supporting Information

Hatta, M., Measures, C. I., Wu, J., Roshan, S., Fitzsimmons, J. N., Sedwick, P. N., & Morton, P. L. (2015). An overview of dissolved Fe and Mn distributions during the 2010–2011 US GEOTRACES North Atlantic cruises: Geotraces GA03. *Deep Sea Research Part II: Topical Studies in Oceanography*, *116*, 117–129. https://doi.org/10.1016/j.dsr2.2014.07.005

Kipp, L. E., Sanial, V., Henderson, P. B., van Beek, P., Reyss, J. L., Hammond, D. E., et al. (2018). Radium isotopes as tracers of hydrothermal inputs and neutrally buoyant plume dynamics in the deep ocean. *Marine Chemistry*, *201*, 51–65. https://doi.org/10.1016/j.marchem.2017.06.011

Mahowald, N. M., Baker, A. R., Bergametti, G., Brooks, N., Duce, R. A., Jickells, T. D., et al. (2005). Atmospheric global dust cycle and iron inputs to the ocean. *Global Biogeochemical Cycles*, *19*(4). https://doi.org/10.1029/2004gb002402

Mandernack, K. W., & Tebo, B. M. (1993). Manganese scavenging and oxidation at hydrothermal vents and in vent plumes. *Geochimica et Cosmochimica Acta*, *57*(16), 3907–3923. https://doi.org/10.1016/0016-7037(93)90343-U

Marsay, C. M., Kadko, D., Landing, W. M., Morton, P. L., Summers, B. A., & Buck, C. S. (2018). Concentrations, provenance and flux of aerosol trace elements during US GEOTRACES Western Arctic cruise GN01. *Chemical Geology*, *502*, 1–14. https://doi.org/10.1016/j.chemgeo.2018.06.007

Resing, J. A., Sedwick, P. N., German, C. R., Jenkins, W. J., Moffett, J. W., Sohst, B. M., & Tagliabue, A. (2015). Basin-scale transport of hydrothermal dissolved metals across the South Pacific Ocean. *Nature*, *523*(7559), 200–203. https://doi.org/10.1038/nature14577